

Pyridyldiimine macrocyclic ligands: Influences of template ion, linker length and imine substitution on ligand synthesis, structure and redox properties



Laura M. Thierer, Qiuran Wang, Sam H. Brooks, Peng Cui, Jia Qi, Michael R. Gau, Brian C. Manor, Patrick J. Carroll, Neil C. Tomson*

University of Pennsylvania, USA

ARTICLE INFO

Article history:

Received 7 November 2020

Accepted 13 January 2021

Available online 30 January 2021

Keywords:

Macrocyclic

Templated synthesis

Redox-active ligand

ABSTRACT

A series of 2,6-diiminopyridine-derived macrocyclic ligands have been synthesized via [2 + 2] condensation around alkaline earth metal triflate salts. The inclusion of a *tert*-butyl group at the 4-position of the pyridine ring of the macrocyclic synthons results in macrocyclic complexes that are soluble in common organic solvents, thereby enabling a systematic comparison of the physical properties of the complexes by NMR spectroscopy, mass spectrometry, solution-phase UV–Vis spectroscopy, cyclic voltammetry and single-crystal X-ray crystallography. Solid-state structures determined crystallographically demonstrate increased twisting in the ligand, concurrent with either a decrease in ion size or an increase in macrocycle ring size (18, 20, or 22 membered rings). The degree of folding and twisting within the macrocycle can be quantified using parameters derived from the $N_{\text{pyr}}\text{-M-N}_{\text{pyr}}$ bond angle and the relative orientation of the pyridinediimine (PDI) and pyridinedialdimine (PDAI) fragments to each other within the solid state structures. Cyclic voltammetry and UV–Vis spectroscopy were used to compare the relative energies of the imine π^* orbital of the redox active PDI and PDAI components in the macrocycle when coordinated to redox inactive metals. Both methods indicate the change from a methyl to hydrogen substitution on the imine carbon lowers the energy of the ligand π^* system.

© 2021 Elsevier Ltd. All rights reserved.

1. Introduction

Rational ligand design has been used in the past to create molecular complexes containing multiple metal centers, and the resulting complexes have been applied toward polymer synthesis [1–4], organic transformations [5–9], and small molecule activation chemistry [10–15]. Some bimetallic, homogeneous molecular complexes have also served to elucidate the roles of metal–metal interactions in enzymatic processes [16–21] and heterogeneous catalyst surfaces [20,22,23]. To further enable these efforts, new generations of ligands that are able to kinetically stabilize multiple metal centers in close proximity to one another are needed. Macrocyclic ligands are promising options for creating complexes to advance these objectives [24,25]. In addition to the kinetic stability offered by the ring structure, the number of atoms constructing the macrocyclic ring may be modified as a way to modulate the dis-

tance between two metal centers. Recently, our group reported the synthesis of two versions of a Schiff base macrocycle that was synthesized via templation around $\text{Sr}(\text{OTf})_2$. These ligands provided facile transmetalation to form dinuclear transition metal complexes that have displayed unique chemistry under highly reducing conditions [26–28]. We have therefore endeavored to systematically explore the synthesis of these macrocycles by pairing of the size of the templating ion with the size of the macrocycle pocket.

Macrocyclic ligands have a long history in the study of coordination chemistry [29], and the [2 + 2] Schiff base condensation of pyridyldiketone fragments with α,ω -diamines around alkaline earth metal cations (Ca^{2+} , Sr^{2+} , Ba^{2+}) was one of the early synthetic methods [30–32]. These pyridyldiimine-based (PDI-based) ligands (Fig. 1) exhibited poor solubility in common organic solvents, thereby limiting structural information to a few crystal structures [31–34] and characterization data to primarily solid-state spectroscopic techniques. The use of coordinating groups with distinct infrared spectroscopy signatures were used in many cases to extrapolate structural data [30,32,35]. Later efforts using linkers with embedded amino, ether and thioether groups (Fig. 1, bottom

* Corresponding author at: Roy and Diana Vagelos Laboratories, Department of Chemistry, University of Pennsylvania, 231 South 34th Street, Philadelphia, PA 19104, USA.

E-mail address: tomson@upenn.edu (N.C. Tomson).

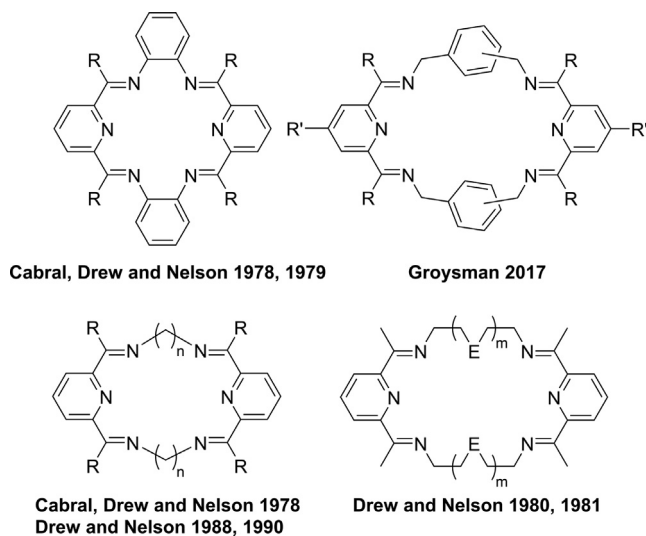
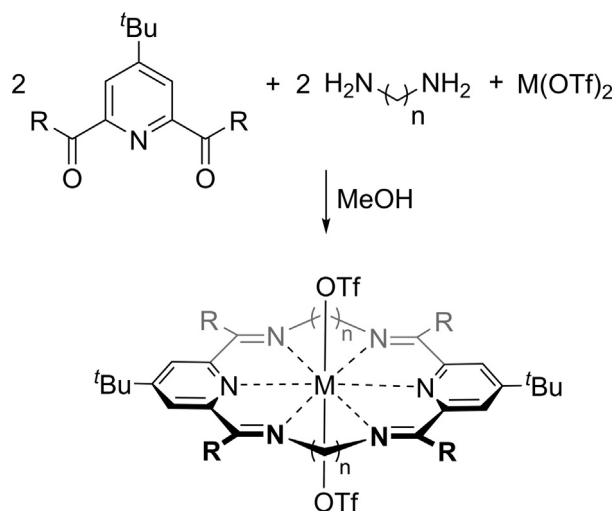


Fig. 1. Examples of pyridyldiimine-based macrocyclic ligands that have been constructed via [2 + 2] Schiff base condensation around Lewis acidic, redox-inactive template ions: R = H, Me; R' = H, *tert*-butyl; n = 2–6; m = 1, 2; E = NH, O, S.

right) provided more crystallographic data but also introduced problems, including the formation of cyclic aminals and the blocking of coordination sites on the resulting bimetallic transition metal complexes [30,35–38]. Separate work was conducted during this time using lanthanide and actinide template ions for macrocycle formation [39]. Given the interest in ligands that can aid chemical transformations involving multiple metal centers and the elucidation of the redox activity of the PDI ligand, which has evolved since the original work with these macrocyclic ligands, interest has grown in revisiting the syntheses of these PDI constructed macrocycles [40,41]. It was previously observed for the templated synthesis of Schiff-based containing macrocycles that optimized reaction conditions can vary significantly based upon the different sizes of macrocycles, the nature of the linkers and the identity of the template ion. This variability has led to the empirical development of optimal synthetic procedures [42].

Herein is reported a series of PDI macrocycles that have been constructed with pocket sizes of 18, 20 and 22 atoms via [2 + 2] Schiff base condensation reactions around alkaline earth metal tri-



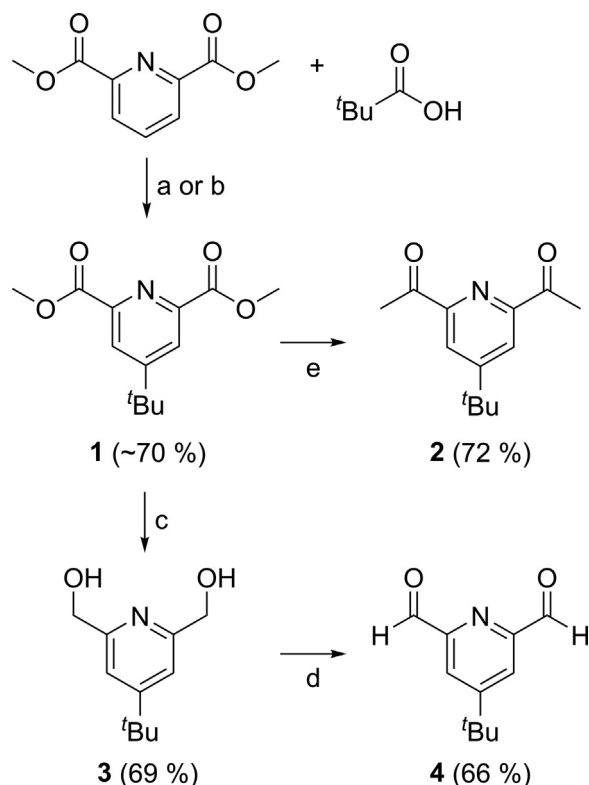
Scheme 1. Synthesis of $(^n\text{PD}(\text{A})_2)\text{M}(\text{OTf})_2$ macrocycles. M = Ca, Sr, Ba; R = H (PDAl) or Me (PDI); n = 2, 3 or 4.

flate salts (Scheme 1). The ligands are noted using the convention of $^n\text{PDI}_2$, where the superscript “n” (n = 2, 3) denotes the number of methylene linkers in the alkyl chains connecting two PDI fragments. The corresponding $^n\text{PDAl}_2$ (n = 2, 3, 4) notation is used to designate the analogous pyridyldialdimine macrocycles. The combination of solubilizing triflate counterions and *tert*-butyl groups at the 4-positions of the pyridyl rings allowed for a systematic investigation into the synthesis and characterization of these species both in the solid- and solution-states. Complete characterization by NMR spectroscopy, mass spectrometry, UV–Vis spectroscopy, cyclic voltammetry and single crystal X-ray crystallography has enabled a more complete understanding of the effects the choice in template ion and imine substitution impart on the synthesis of these macrocycles as well as the structural and electronic features of the complexes.

2. Results and discussion

2.1. Synthesis of precursors

This chemistry commences with the addition of a *tert*-butyl group to dimethyl pyridine-2,6-carboxylate under Minisci conditions. Our procedure was adapted from those for the *tert*-butylation of 2,6-diacetylpyridine (both with [43] and without [44] the use of chlorobenzene) to provide a synthetic path to 4-*tert*-butylpyridine-dimethyl-2,6-dicarboxylate (**1**, Scheme 2) [45]. The reduction of **1** using a Claisen condensation with ethyl acetate, followed by acid-promoted decarboxylation [46] affords a novel route to 4-*tert*-butyl-2,6-diacetylpyridine (**2**) that uses inexpensive starting materials [43,44]. Alternatively, **1** can be reduced with NaBH_4



Scheme 2. Synthetic path to obtain 4-*tert*-butylpyridine-2,6-dicarboxylate (**1**) and conversion to either 4-*tert*-butyl-2,6-diacetylpyridine (**2**) or 4-*tert*-butyl-2,6-diformylpyridine (**4**) via 4-(*tert*-butyl)pyridine-2,6-diyldimethanol (**3**): (a) AgNO_3 , H_2SO_4 , $\text{Na}_2\text{S}_2\text{O}_8$, H_2O , PhCl, reflux 6 h; (b) AgNO_3 , H_2SO_4 , $\text{Na}_2\text{S}_2\text{O}_8$, H_2O , rt 18 h; (c) NaBH_4 , EtOH, 0 °C to reflux 12 h; (d) SeO_2 , dioxane, reflux 6 h; (e) 1. NaOEt, EtOAc, reflux 6 h, 2. HCl, reflux 18 h.

[47], to provide the novel (4-*tert*-butylpyridine-2,6-diyl)dimethanol (**3**), which can be subsequently oxidized with SeO₂ [48] to obtain 4-*tert*-butyl-2,6-diformylpyridine (**4**, Scheme 2). Each synthetic step can be completed on > 10 g scale with yields of > 65 %.

2.2. Macrocyclic synthesis

[2 + 2] Schiff base condensation of either **2** or **4** with an α,ω -diamine in the presence of Ca(OTf)₂, Sr(OTf)₂ or Ba(OTf)₂ afforded the desired series of macrocyclic complexes (Scheme 1) in yields of 50–95 %. The products are referred to below according to the notation ⁿR[M], where **n** is the length of the aliphatic linker (n = 2, 3, 4), **R** is the identity of the imine-carbon substituent (R = H, Me), and **M** represents the identity of the inorganic salt (M = Ca(OTf)₂, Sr(OTf)₂, Ba(OTf)₂). A comparison of complexes ²Me[Ca], ²Me[Sr], ³H[Ba] and ⁴H[Ba] to literature reports of comparable macrocycles using perchlorate salts and without the added *tert*-butyl group indicates improvements in yields by 10–40 % [31,32]. A previous mechanistic study proposed that product yields could be affected by the solubility of the partially constructed macrocycle fragments [30]; therefore, the higher yields obtained when using more soluble pyridyl synthons and alkaline earth triflate salts support this proposal. Additionally, it is conceivable that the pyridyldicarbonyl moieties bind to the alkaline earth ions prior to condensation with the diamine. This would serve to both activate the carbonyl towards nucleophilic attack and, upon ligation of the diamine, generate a high local concentration of carbonyl groups relative to the amine, thereby favoring [2 + 2] macrocycle formation. Therefore, a 15 min mix time of **2/4** and the triflate salt was added to the synthesis prior to the addition of the amine in an effort to increase product yields. Lastly, replacement of perchlorate anions with triflate salts serves to mitigate the safety concerns associated with the perchlorates [49], enabling safe, multi-gram scale syntheses of these macrocycles.

Templating ions are used during macrocycle syntheses in order to favor ring closure over polymer formation via kinetic templating effects [31]. Reports in the literature have used electrospray ionization mass spectrometry (ESI-MS) to identify reaction intermediates [50–52]; therefore, we aimed to use this technique to explore the intermediates formed during the macrocyclization process. Each of the triflate salts and either **2** or **4** were stirred together in methanol at room temperature for 15 min, and the resulting solutions were analyzed by ESI-MS. The mass spectra of these solutions presented peaks consistent with the *m/z* ratios for [2₂M(OTf)]⁺ and [4₂M(OTf)(MeOH)_{1–4}]⁺, respectively (see SI section IV), suggesting the initial stir time does allow **2/4** to chelate to the template ion. The lack of coordinated methanol when using **2** may be attributed to the modest increase in steric bulk from the methyl substituents on the imine, constraining the available coordination space around the ion. Also, notable is the presence of the singly coordinated [2₁M(OTf)]⁺ species in the mass spectra, while [4₁M(OTf)]⁺ species were not identified. Despite the observation of [2₁M(OTf)]⁺, the resulting [2 + 2] ⁿPDI₂ macrocycle products were obtained in high yields (most > 90 %), supporting prior proposals that the templating ion is able to inhibit the formation of polymeric materials.

The synthesis of the ⁿPDI₂ macrocycles painted a slightly different story from the ⁿPDI₂ counterparts. Operating the ⁿPDI₂ synthesis reactions at reflux, particularly for the largest ⁴PDI₂ macrocycles, resulted in a significant quantity of insoluble material (presumably polymers). Yields for the ⁴PDI₂ products were improved and insoluble byproducts were reduced when both the concentration of the starting materials in solution was decreased and the reaction temperature was changed from reflux to room temperature. These changes in optimal reaction conditions between the ⁿPDI₂ and ⁿPDI₂ macrocycles suggest an increased kinetic accessibility of the aldehyde towards nucleophilic attack.

This rationale may also explain the ability to readily form ⁴PDI₂ macrocycles, while the corresponding ⁴PDI₂ ligand remains elusive in our hands.

The addition of a *tert*-butyl group to the pyridyl ring resulted in the desired improvement in the solubility of the macrocycles. The ⁿPDI₂ (n = 2, 3) complexes were readily soluble in chloroform, dichloromethane, THF and even sparingly soluble in toluene. The change from methyl to hydrogen substitutions on the imine carbons in the corresponding ⁿPDI₂ (n = 2, 3) complexes, particularly for ²H[Sr] and ³H[Sr], resulted in a markedly less soluble set of macrocycles, which were sparingly soluble in THF and more soluble in acetonitrile and methanol. A modest improvement in solubility was observed for ³H[Ca] and ³H[Ba], with both being marginally soluble in dichloromethane and more readily soluble in THF than their strontium triflate counterparts. Contrastingly, the ⁴PDI₂ complexes are easily dissolved in THF, chloroform and dichloromethane. The influence of alkyl linker length on solubility may explain why the addition of a *tert*-butyl group to a set of arene-bridged PDI macrocyclic complexes did not demonstrate the marked change in solubility observed here [41]. The present series suggests solubility may be a more important factor towards formation of product than the relative size of the template ion (*vide infra*).

2.3. Structural description

The solid-state structures of all complexes were determined using single crystal X-ray diffraction (see SI section III). In all cases, the macrocyclic ligands are hexadentate with respect to the templating cation, while the two triflate anions bind in a 2κ¹O (2^{Me}[Ca], 2^{Me}[Sr], 3^H[Ca], 4^H[Sr]), 1κ¹O,1κ²O,O' (3^{Me}[Sr], 3^{Me}[Ba], 2^H[Ca], 2^H[Sr]) or 2κ²O,O' (3^H[Sr], 3^H[Ba], 4^H[Ba]) fashion, resulting in coordination numbers around the template ion that range from 8 to 10 (see Fig. 2 for examples and SI section III for complete information). These coordination numbers are consistent with the reported primary coordination sphere of the aquo ions, which are best described as [Ca(H₂O)₈]²⁺, [Sr(H₂O)₈]²⁺, and [Ba(H₂O)₈]²⁺ [53]. The M-N bond lengths are consistent with reported crystal structures of related molecules [31,32,36]. The aquo ions also serve as a benchmark for the relative size of the cations, with M-O distances of 2.79 Å for Ba²⁺, 2.62 Å for Sr²⁺, and 2.33–2.41 Å for Ca²⁺ [53].

Attempts were made to template the smallest ²PDI₂ macrocycle with Mg(OTf)₂ under the same conditions used to form ²Me[Ca] and ²Me[Sr], however these attempts were unsuccessful, consistent with previous reports of Mg²⁺ being an ineffective template ion [31,36]. Our structural data adds additional evidence to the possibility that the coordination sphere of Mg²⁺ is unable to accommodate the required 8–10 chelating groups required to support macrocycle formation. The Mg²⁺ aquo ion is representative of this smaller coordination sphere, with a coordination number of 6 in the reported [Mg(H₂O)₆]²⁺ species and a smaller 2.00–2.15 Å Mg-O bond length [53].

With the exception of ³Me[Ca] and ⁴H[Sr], the six nitrogen atoms occupy positions around the metal that are best described as equatorial, while the two triflate anions coordinate *trans* to each other, resembling an axial arrangement. Complex ³Me[Ca] also demonstrates the roughly equatorial arrangement of the nitrogen atoms on the macrocycle, but methanol molecules coordinate in the nominally axial positions, while the triflate anions reside in the outer coordination sphere (see Fig. 3). These two coordinated methanol molecules are an artifact of the crystallization from methanol, as the powdered material isolated during synthesis does not show the presence of methanol by NMR spectroscopy, IR spectroscopy or elemental analysis. Attempts to grow crystals of ³Me[Ca] from non-coordinating solvents such as dichloromethane, dichloror-

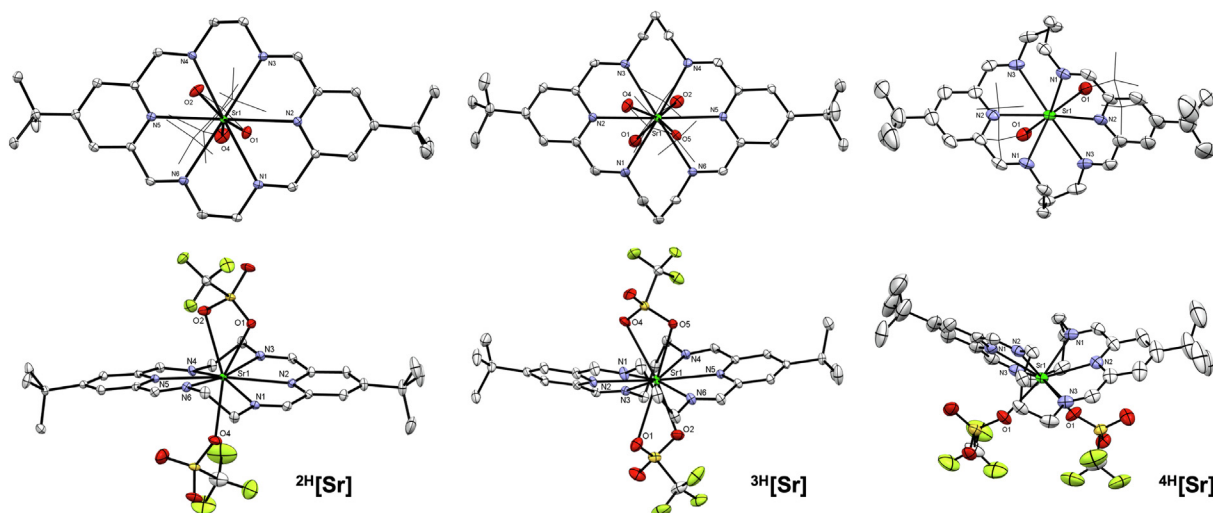


Fig. 2. ORTEP diagrams for the $(^n\text{PDAI}_2)\text{Sr}(\text{OTf})_2$ complexes ($^{2\text{H}}[\text{Sr}]$, $^{3\text{H}}[\text{Sr}]$ and $^{4\text{H}}[\text{Sr}]$). Thermal ellipsoids are shown at 50 % probability level. Hydrogens, disordered atoms, and co-crystallized solvent molecules are omitted for clarity. On the top structures the non-coordinating atoms in the triflate ions are depicted in wire frame to highlight the coordination around the strontium atom.

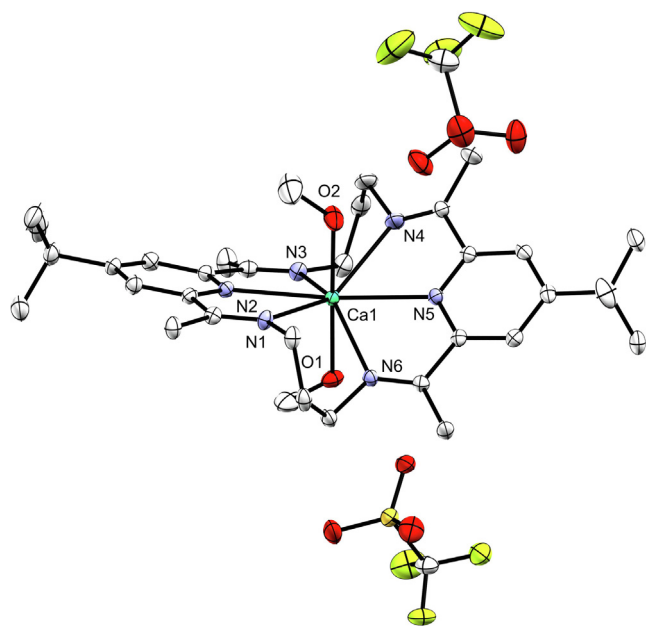


Fig. 3. ORTEP diagram for the $([^3\text{PDI}_2]\text{Ca}(\text{MeOH})_2)[\text{OTf}]_2$ complex ($^{3\text{Me}}[\text{Ca}]$). Two methanol molecules coordinate to calcium, causing the two triflate counter ions to reside in the outer coordination sphere. Thermal ellipsoids are shown at the 50 % probability level. Hydrogens, disordered atoms and a co-crystallized diethyl ether molecule are omitted for clarity.

ethane or toluene resulted in material of insufficient quality for crystallographic analysis.

Complex $^{4\text{H}}[\text{Sr}]$ presents somewhat differently, with the two triflate anions lying on the same side of the macrocycle due to a high degree of ligand twisting that causes the PDI moieties to orient in an almost perpendicular arrangement (see Fig. 2, right). This difference in orientation for $^{4\text{H}}[\text{Sr}]$ appears to be adopted to maintain equivalent coordination to all six nitrogen donors in the macrocycle when pairing the large macrocycle pocket with the smaller strontium cation.

The neutral oxidation state of these macrocyclic $^n\text{PD(A)}_2$ ligands can be inferred from characteristic bond lengths within the PD(A)I moieties [54]. It is further supported by the IR spectro-

scopic data for most of the complexes, which showed sharp features at $ca. 1600\text{ cm}^{-1}$ and less intense features between 1640 and 1660 cm^{-1} (see Table 1). These values are in the range for vibrations assigned to C=N stretches (from both the imine and pyridine) in other metal coordinated mononuclear PDI⁰ complexes [55,56] and the previously reported alkaline earth metal templated macrocycles [30–32,36,37,57].

2.4. Pocket size and template ion

Inspection of the angle formed between the two planes defined by the PD(A) fragments within the macrocycle (dihedral angle, φ , Fig. 4 top) revealed a problem when describing the nature of the distortion required to coordinate the ligand to the templating ion. The angle φ generates a unique geometric description of chemical systems only when the two planes under inspection share a common bond. Without this shared bond, the orientation of a molecular fragment on one plane is undetermined with respect to a molecular fragment on another. In the present case, two additional pieces of information are needed in order to define the orientation of the molecular fragments on their respective planes. The first is a vector for each fragment that can be used to orient the molecular fragments on their respective planes. This vector will be used to determine the inclination of the rings with respect to one another, with the angle between these vectors providing a convenient metric given that the macrocyclic geometry imposes natural constraints on the range of possible vector orientations (Fig. 4, bottom). The second parameter is a definition of the distance between the molecular fragments. We will define the distance term by using the average M-N_{pyr} bond lengths (r_{MN}). Since this vector also determines the orientation of each pyridyl ring on its local plane, then the inclination of the pyridyl rings with respect to one another may be approximated using the angle between the M-N_{pyr} vectors. This allows for use of the deviation of N_{pyr}-M-N_{pyr} from 180° as our final identifying term, the folding angle (θ).

Comparison of the $^{2\text{Me}}[\text{Sr}]$ and $^{2\text{Me}}[\text{Ca}]$ structures demonstrates how these metrics can be used to describe the ligand contortion that can be observed upon the change to a smaller template ion (Sr^{2+} to Ca^{2+}). Complex $^{2\text{Me}}[\text{Sr}]$ is the only structure in which the planes defined by the PD(A)I fragments are parallel ($\theta = \varphi = 0^\circ$, see Table 1 and Fig. 5 left). The change to the smaller calcium ion

Table 1
IR and select structural information for macrocyclic complexes.

	Complex	Avg. r_{M-N}^b (Å)	Folding Angle ^c (θ , °)	Dihedral Angle ^d (φ , °)	ν_{C-N} (cm ⁻¹)
² Me[Ca]	(² PDl ₂)Ca(OTf) ₂	2.63	25.7	68.3	1603, 1647
² Me[Sr]	(² PDl ₂)Sr(OTf) ₂	2.76	0.0	0.0	1601, 1642
³ Me[Ca]	[(³ PDl ₂)Ca(MeOH) ₂][OTf] ₂	2.61	6.7	50.3	1603, 1655
³ Me[Sr]	(³ PDl ₂)Sr(OTf) ₂ ^a	2.71	2.4	47.2	1602, 1644
³ Me[Ba]	(³ PDl ₂)Ba(OTf) ₂	2.86	30.3	48.7	1597
² H[Ca]	(² PDAI ₂)Ca(OTf) ₂	2.65	6.8	16.3	1606, 1663
² H[Sr]	(² PDAI ₂)Sr(OTf) ₂	2.70	7.1	14.0	1602, 1656
³ H[Ca]	(³ PDAI ₂)Ca(OTf) ₂	2.62	1.4	41.2	1602, 1660
³ H[Sr]	(³ PDAI ₂)Sr(OTf) ₂	2.71	4.0	38.9	1600, 1660
³ H[Ba]	(³ PDAI ₂)Ba(OTf) ₂	2.87	10.8	34.6	1595
⁴ H[Sr]	(⁴ PDAI ₂)Sr(OTf) ₂	2.68	73.4	63.0	1600
⁴ H[Ba]	(⁴ PDAI ₂)Ba(OTf) ₂	2.94	14.6	49.4	1597, 1654

^aCrystallographic data for ²Me[Sr] and ³Me[Sr] have been previously reported [26]. ^bAverage bond distances for the M-N_{pyr} bonds. ^cFolding angle is defined as the deviation of N_{pyr}-M-N_{pyr} from 180°. ^dDihedral angle is defined as the angle formed between the two planes comprising each pyridinediimine moiety.

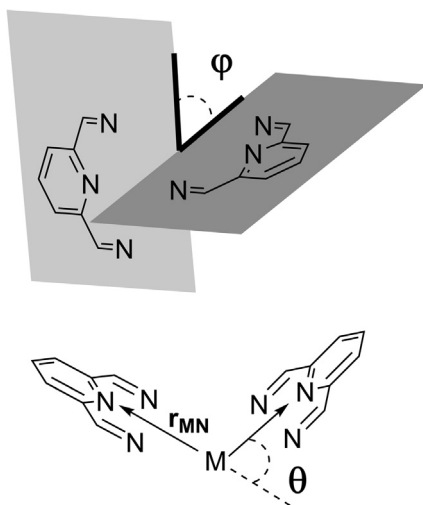


Fig. 4. Depiction of the three metrics (φ , r_{MN} and θ) used to describe the orientation of the macrocyclic ligand around the template ion.

in ²Me[Ca] results in a dramatic change in conformation ($\theta = 25.7^\circ$, $\varphi = 68.3^\circ$) as the ligand contorts to maintain coordination of the nitrogen atoms to the ion ($r_{MN} = 2.63$ Å for ²Me[Ca] vs. 2.76 Å for ²Me[Sr]; Fig. 5). Similarly, inspection of the structures for the complexes ²H[Sr], ³H[Sr] and ⁴H[Sr] demonstrate the increases in distortion available to this system as the ring size changes about a single metal ion, from a modest ripple for ²H[Sr] ($\theta = 7.1^\circ$, $\varphi = 14.0^\circ$), to a more distinct change in dihedral angle for ³H[Sr] ($\theta = 4.0^\circ$, $\varphi = 38.9^\circ$), to a pronounced fold ($\theta = 73.4^\circ$) and twist ($\varphi = 63.0^\circ$) for the largest macrocycle, ⁴H[Sr] (Fig. 2).

Notably, the Sr-N bond distances remain similar across all the ⁿH[Sr] complexes (Tables 1 and S7) and within the 2.5–3.1 Å range for Sr-N_{py} and Sr-N_{imine} distances reported in the CCDC database [58]. The flexibility in the alkyl linkers accommodates the increase in macrocycle pocket size to allow for equivalent bonding for all six nitrogens in the macrocycle. This in turn is enabled by the electrostatic bonding interaction between the alkaline earth metal cation and the PD(A)I ligand to accommodate nitrogens occupying different positions around the circumference of the ion while maintaining the same degree of bonding interaction. The change to either a more rigid linker, such as recently reported aryl examples [40,41], or the choice of other main group template ions [31], may constrain the system enough to impede macrocycle formation. These added constraints may explain why one literature example using a rigid *o*-phenylenediamine linker with a cadmium template ion was not successful when the barium ion could be employed effec-

tively [35]. Therefore, while this series has proven somewhat robust to the selection of template ion due to the flexible alkyl linkers, other systems may prove more sensitive to template ion choice.

In order to probe for the extent to which the twisting and folding observed in the solid state persists in solution, we turned to ¹H NMR spectroscopic analysis. ¹H NMR spectra of ⁴H[Sr] and ⁴H[Ba] indicate equivalency in the respective imine and pyridine signals as well as two broadened features for the hydrogens on the bridging methylene groups. Based upon the solid-state structures, the twisting observed in the alkyl linkers differentiates the geminal protons on each of the two unique methylene carbons (see Scheme 3). If this structure were static in solution, the expectation would be to observe diastereotopic signals in the NMR spectra for each of these protons, H_a, H_b, H_c and H_d. Since only a single, broadened signal is observed for each set of methylene groups (H_a = H_b and H_c = H_d), the ¹H NMR spectroscopic data indicate that the twisting of the macrocycles around the template ion is fluxional, with a rate on the order of the NMR timescale at 25 °C.

This fluxional change in coordination around the template ion would require overcoming an energy barrier to complete the exchange process, therefore the ¹H NMR spectroscopic signals for the hydrogens on the alkyl linkers of ⁴H[Sr] and ⁴H[Ba] were monitored as the temperature was lowered. At the coalescence temperatures (T_c) of 275 K and 215 K for ⁴H[Sr] and ⁴H[Ba] respectively, broad proton signals resolved into distinct features as the rate of exchange slowed with respect to the NMR timescale (Figs. S118 and S119). The signals for H_a and H_b were used to calculate the activation energies for the exchange processes of ⁴H[Sr] ($\Delta G^\ddagger = 12.7$ kcal/mol) and ⁴H[Ba] ($\Delta G^\ddagger = 9.8$ kcal/mol) [59]. The overall modest energies involved, even for this highly distorted macrocyclic ligand, indicates facile changes to coordination around the template ion in solution.

2.5. Electrochemical characterization

The electrochemical behaviors of ²Me[Sr], ³Me[Ca], ³Me[Sr], ³Me[Ba], ⁴H[Sr], and ⁴H[Ba] were probed using cyclic voltammetry. All experiments were completed in THF solutions with [*n*-Bu₄N][PF₆] as the supporting electrolyte. A glassy carbon working electrode and Ag/Ag⁺ pseudoreference electrode were used, with all features referenced internally to the ferrocene/ferrocenium (Fc/Fc⁺) redox couple.

Scans between +1.5 and -3.5 V (at a scan rate of 100 mV/s) revealed close-lying reduction features at ca. -2.0 V and additional features near -3.0 V (see SI section VII). Only ³Me[Ca] and ⁴H[Sr] showed redox features that might be classified as quasireversible, but the measurements are unstable upon multiple scans, indicat-

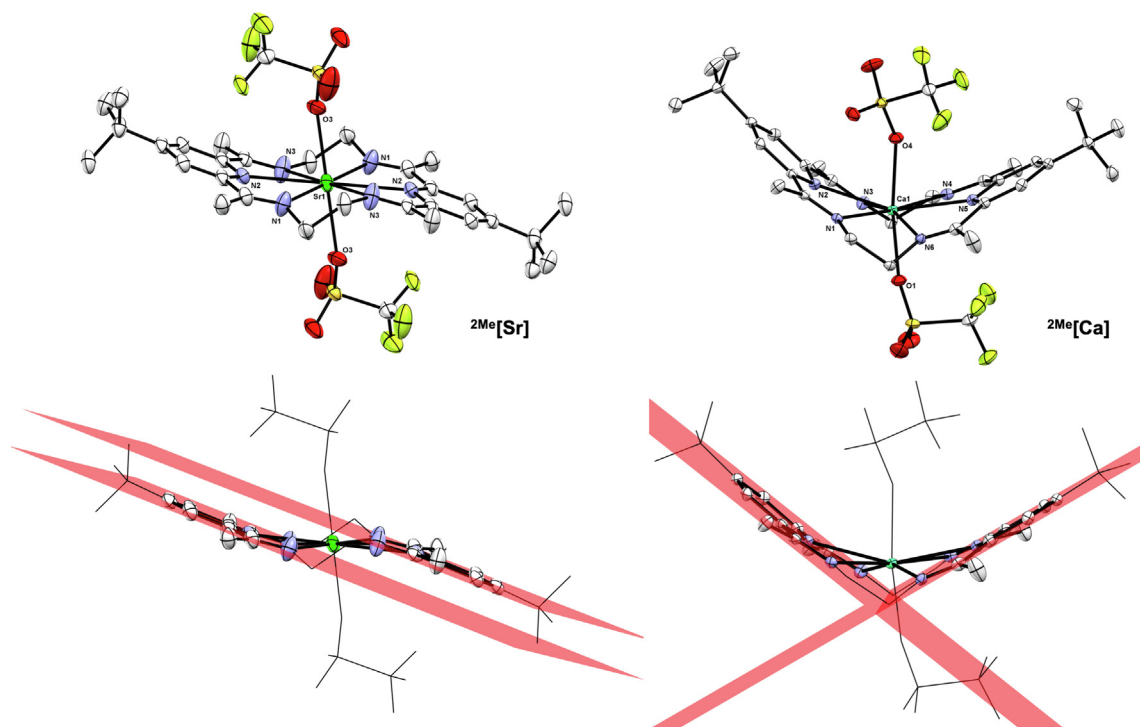
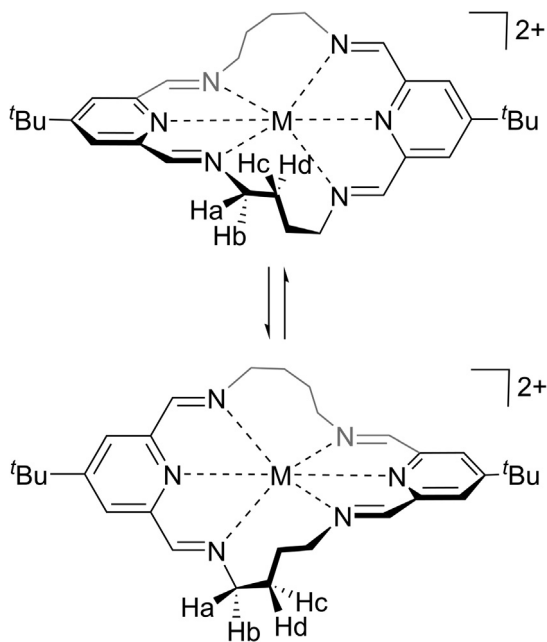


Fig. 5. Top: ORTEP diagram for the $[(^2\text{PDI})\text{M}][\text{OTf}]_2$ complexes ($^{2\text{Me}}[\text{Ca}]$ and $^{2\text{Me}}[\text{Sr}]$). Thermal ellipsoids are shown at 50 % probability level. Hydrogens, disordered atoms and co-crystallized solvent molecules are omitted for clarity.



Scheme 3. Depiction of the interconversion between the helical enantiomers for $^{4\text{H}}[\text{Sr}]$ and $^{4\text{H}}[\text{Ba}]$ (top, Δ isomer; bottom, Λ isomer) proposed to account for the equivalent ^1H NMR spectroscopic signals for H_a and H_b as well as H_c and H_d .

ing these species are not freely diffusing and/or are fouling the electrode surface over the course of the experiment. All the remaining complexes show completely irreversible behavior, with oxidation events (if observed at all) that were much less intense than the reduction features and were separated from the reduction events by greater than 100 mV. Similarly irreversible features have been observed in a mononuclear $(^{\text{ph}}\text{PDI})\text{ZnCl}_2$ complex, where the irreversibility was attributed to the loss of chloride ligands upon

reduction [60]. The loss of the triflate anion(s) upon reduction of these macrocyclic ligands is also likely, which could be leading to the irreversible electrochemical behavior.

In order to resolve the close-lying reduction features, we turned to square-wave voltammetry (see Fig. 6, and the SI section VII). The reduction features for all complexes follow a similar pattern of two sets of two close lying reduction features, with separations of less than 140 mV within each set (see Table 2 and Fig. 6). The reduction values for the ligands do not change significantly based upon either the identity of the metal or the size of the macrocyclic pocket.

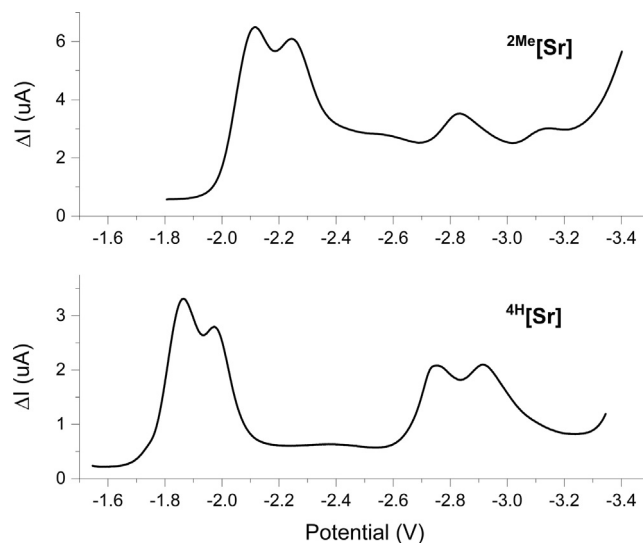


Fig. 6. Square wave voltammograms plotting the change in current (ΔI) vs. potential for complexes $^{2\text{Me}}[\text{Sr}]$ and $^{4\text{H}}[\text{Sr}]$. Solvent THF, supporting electrolyte $[n\text{-Bu}_4\text{N}][\text{PF}_6]$, glassy carbon working electrode, Ag/Ag^+ pseudo reference, referenced to Fc/Fc^+ .

Table 2
Reduction events measured by square wave cyclic voltammetry.

	Reduction 1 (V)	Reduction 2 (V)	Reduction 3 (V)	Reduction 4 (V)
$^{2\text{Me}}[\text{Sr}]$	-2.11	-2.24	-2.83	-3.14
$^{3\text{Me}}[\text{Ca}]$	-2.10	-2.23	-3.02	-3.27
$^{3\text{Me}}[\text{Sr}]$	-2.11	-2.24	-3.01	-3.36
$^{3\text{Me}}[\text{Ba}]$	-2.16	-2.29	-3.01	-3.30
$^{3\text{H}}[\text{Sr}]$	-1.91	-1.99	-2.71	-2.89
$^{4\text{H}}[\text{Sr}]$	-1.86	-1.97	-2.75	-2.91
$^{4\text{H}}[\text{Ba}]$	-1.91	-2.04	-2.74	-2.90

Comparison of the first feature for the $^{\text{nMe}}[\text{M}]$ complexes to the first feature in the $^{\text{nH}}[\text{M}]$ counterparts demonstrates a *ca.* 0.2 V shift to more cathodic reduction potentials (Table 2) for the $^{\text{nMe}}[\text{M}]$ derivatives. Comparison of these data to a reported mononuclear, phenyl-substituted imine complex ($^{\text{Ph}}\text{PDI})\text{ZnCl}_2$, that has a first reduction occurring at -1.65 V [60], indicates the ligand reduction potential shifts to more cathodic values concurrent with the change to more electron-donating substituents on the imine carbon.

The four observed reduction features are most likely associated with successive, one-electron reductions of the macrocycles (Fig. 7). Each PD(A)I fragment contains two low-lying π^* orbitals that have been shown to undergo discrete redox-chemistry when bound to metal ions. This creates the possibility in $^{\text{n}}\text{PD(A)}_2$ that each observed electrochemical step could correspond to a two-electron reduction process, however, qualitative inspection of the both the cyclic voltammograms and square wave voltammograms against a known quantity of ferrocene as an internal standard would require a 4x increase in intensity of the macrocycle peak height in order to approximate the response for a 2 e^- redox process (see Fig. S139) [61]. In the mononuclear complex ($^{\text{Ph}}\text{PDI})\text{ZnCl}_2$, the difference between the first and second redox potential was reported as 0.2 V [60], and other cyclic voltammetry studies of the PDI ligand only report the observation of a maximum of 3 e^- reductions in a single PDI unit [41,62]. It is thus unlikely the complexes reported here are being reduced beyond $[\text{L}_2]^{4-}$ [63].

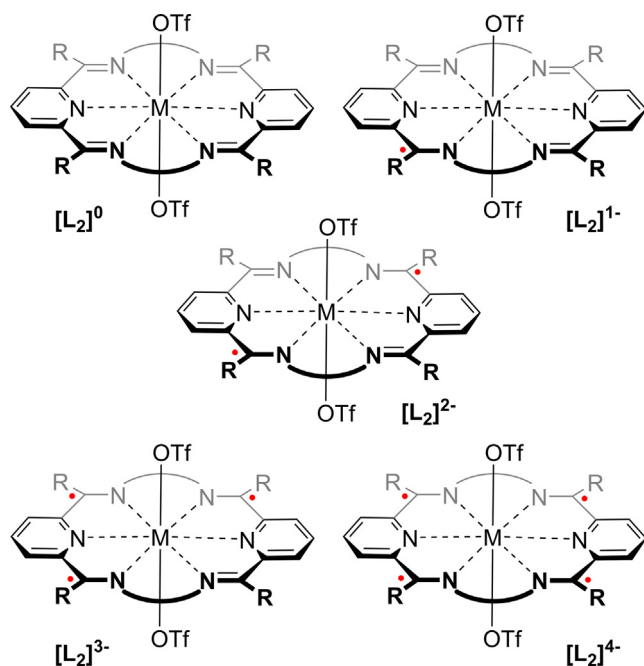


Fig. 7. Depiction of the electron transfer associated with each one e^- ligand reduction event using a simplified structure for clarity; $\text{L}_2 = ^{\text{n}}\text{PD(A)}_2$; $\text{M} = \text{Ca}, \text{Sr}, \text{Ba}$; $\text{R} = \text{H}$ (PDAl) or Me (PDI).

Instead, the close energetic proximity of the first two features is likely due to a modest amount of electrostatic repulsion to the addition of an electron to the second PD(A)I fragment in the macrocycle, leading to two singly reduced PD(A)I units. This is depicted in Fig. 7 as $[\text{L}_2]^{1-}$ corresponding to the first reduction feature and $[\text{L}_2]^{2-}$ in the second reduction feature. Similar independent, one e^- ligand redox events were observed upon reductions of $[\text{ZnL}_2]^{2+}$ complexes, where L is either a PDI ligand [56] or α -iminopyridine ligand [64]. The independent, one e^- ligand reduction features for these complexes were separated by 0.28 V (PDI) and 0.17 V (α -iminopyridine) despite the structural and spectroscopic equivalence of the two ligands within the same complex. The third feature observed for these macrocyclic complexes may be thought of as the second reduction of one of the PD(A)I fragments to form $[\text{L}_2]^{3-}$. The larger difference observed between features 2 and 3 in comparison to 1 and 2 is indicative of the coulombic barrier to doubly reducing one of the PD(A)I fragments. The third feature is then closely followed by a fourth reduction to generate the $[\text{L}_2]^{4-}$ species.

2.6. Electronic absorption spectroscopy

Pyridyldiimine and α -iminopyridine ligands display distinct features in the UV spectral region (200–333 nm, 30,000–50,000 cm^{-1}) attributed to intraligand charge transfer (ILCT) events [56,64,65]. Reported computational efforts with zinc coordinated α -iminopyridine ligands have proposed these transitions to be to ligand based $\pi \rightarrow \pi^*$ transitions [66,67]. The more soluble complexes of this series ($^{2\text{Me}}[\text{Ca}]$, $^{2\text{Me}}[\text{Sr}]$, $^{3\text{Me}}[\text{Ca}]$, $^{3\text{Me}}[\text{Sr}]$, $^{3\text{Me}}[\text{Ba}]$, $^{3\text{H}}[\text{Ca}]$, $^{3\text{H}}[\text{Ba}]$, $^{4\text{H}}[\text{Sr}]$, and $^{4\text{H}}[\text{Ba}]$) were analyzed in THF and dichloromethane to characterize the ILCT features for these macrocycles when coordinated to redox inactive metal ions. Complex $^{2\text{H}}[\text{Sr}]$, with poor to no solubility in THF and dichloromethane, was measured in acetonitrile along with $^{2\text{Me}}[\text{Sr}]$ and $^{3\text{Me}}[\text{Sr}]$. All complexes displayed feature(s) between 30,000–37,000 cm^{-1} (270–333 nm) and at 40500 cm^{-1} (247 nm) as expected based upon literature examples of other PD(A)I complexes coordinated to redox inactive metals [55,65–67]. The wider UV window for acetonitrile allowed for observation of an additional higher energy feature at approximately 45,000 cm^{-1} (222 nm) for three representative complexes, $^{2\text{H}}[\text{Sr}]$, $^{2\text{Me}}[\text{Sr}]$ and $^{3\text{Me}}[\text{Sr}]$. For any individual complex, the change in solvent (THF, dichloromethane or acetonitrile) did not result in an energy change for the absorption features. Within each type of ligand, PDAl or PDI, neither the size of the macrocycle pocket, nor the identity of the template ion changed the energy of the absorption features. However, the change in the imine substitution from hydrogen (PDAl) to methyl (PDI) did result in an observed difference in the lower energy spectral features (30,000–37,000 cm^{-1} , 270–333 nm). Features in this same energy range have been previously observed to shift with changes to the electron donating/withdrawing nature of the aryl group on the imine nitrogen, however attempts were not made to formally assign these transitions [68]. The extension of this analysis to changes in the substitution of the imine carbon are less explored

[69], despite observed reactivity differences [70–72]. Comparing the lower energy features in these macrocyclic ligands, the $n^{M}[M]$ complexes exhibit a single broad signal, while the $n^H[M]$ macrocycles each display a set of three closely overlapping peaks (see Fig. 8). Using $^{2Me}[Sr]$ and $^{4H}[Sr]$ as representative examples, the λ_{max} for $^{4H}[Sr]$ in this region is red shifted by 1400 cm^{-1} relative to the λ_{max} for $^{2Me}[Sr]$.

Revisiting the initial reduction potentials for $^{4H}[Sr]$ and $^{2Me}[Sr]$ observed electrochemically (-1.86 V vs. -2.10 V , respectively), the 0.24 V anodic shift for $^{4H}[Sr]$ corresponds to a 1936 cm^{-1} stabilization of the $^n\text{PDAl}_2\pi^*$ manifold compared to that of $^n\text{PDI}_2$. The similarity of this value to the $\Delta\lambda_{max}$ observed spectroscopically led us to conclude that the donor orbital associated with the absorption event is not part of the π/π^* system. Instead, this experimental observation suggests an ILCT assignment of an $n \rightarrow \pi^*$ transition.

To support the assignment of the electronic transitions occurring with this macrocyclic ligand, time dependent density functional theory (TD-DFT) computational analyses were completed on model compounds $[\text{}^3\text{PDI}_2\text{Sr}]^{2+}$ and $[\text{}^3\text{PDAl}_2\text{Sr}]^{2+}$. These models were built from the crystallographically determined structures of $^{3Me}[Sr]$ and $^{3H}[Sr]$ by truncating the *tert*-butyl groups to hydrogens and removing the triflate groups. The geometries of these model cationic structures were optimized at the B97-D3 level of theory, using the COSMO solvation model (conductor-like screening model) with the dielectric constant of acetonitrile.

The predicted transitions from TD-DFT indicated reasonable agreement with the experimentally measured absorption spectra, including the prediction of a shift in the low energy transitions between the PDI and PDAl macrocycles (Fig. 9). The computational model predicted the lower energy features to occur between $31,000\text{--}36,000\text{ cm}^{-1}$ ($323\text{--}278\text{ nm}$) for $[\text{}^3\text{PDI}_2\text{Sr}]^{2+}$ and $29,000\text{--}35,000\text{ cm}^{-1}$ ($345\text{--}286\text{ nm}$) for $[\text{}^3\text{PDAl}_2\text{Sr}]^{2+}$, with the majority of these features best described as $n \rightarrow \pi^*$ transitions. Numerous transitions were predicted due to the presence of a dense set of linear combinations of the six nitrogen lone pair donor orbitals and acceptor orbitals composed of linear combinations of the redox active $a_2\text{-PD(A)}\text{-}\pi^*$ and $b_1\text{-PD(A)}\text{-}\pi^*$ fragments (Fig. 10, see SI140 for orbital surface diagrams and symmetry of all the n donor orbitals) [73]. Our group has previously reported similar linear combinations of these $\text{PDI-}\pi^*$ fragments in our macrocyclic metal complexes [15,27]. Without additional experimental data, it would be difficult to determine if, and by how much, the “ n ” and “ π^* ”

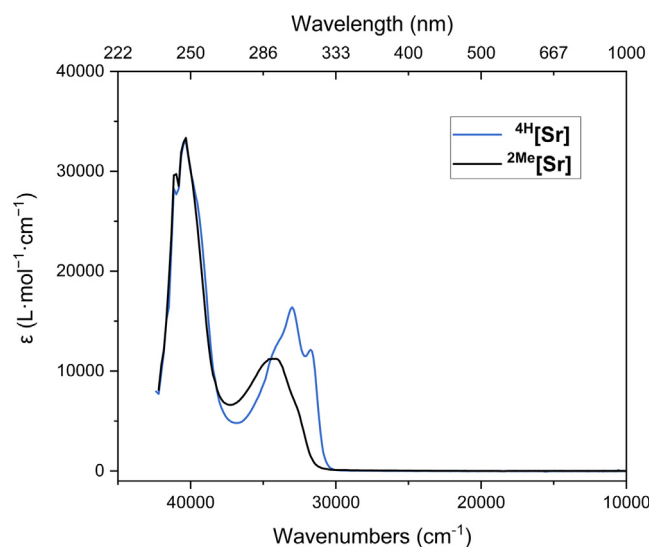


Fig. 8. UV-Vis spectra for complexes $^{4H}[Sr]$ and $^{2Me}[Sr]$ in THF demonstrating the change in the absorption energies with the change from the $^n\text{PDAl}_2$ to $^n\text{PDI}_2$ ligand.

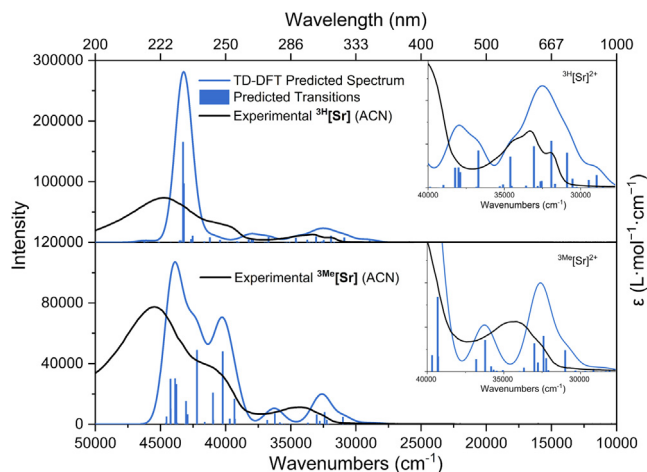


Fig. 9. TD-DFT predicted absorption transitions and spectra for the model compounds $[\text{}^3\text{PDI}_2\text{Sr}]^{2+}$ and $[\text{}^3\text{PDAl}_2\text{Sr}]^{2+}$ with the corresponding experimentally measured data for $^{3Me}[Sr]$ and $^{3H}[Sr]$ in acetonitrile (ACN). Insert: Rescaled graphs highlighting the lower energy electronic transitions.

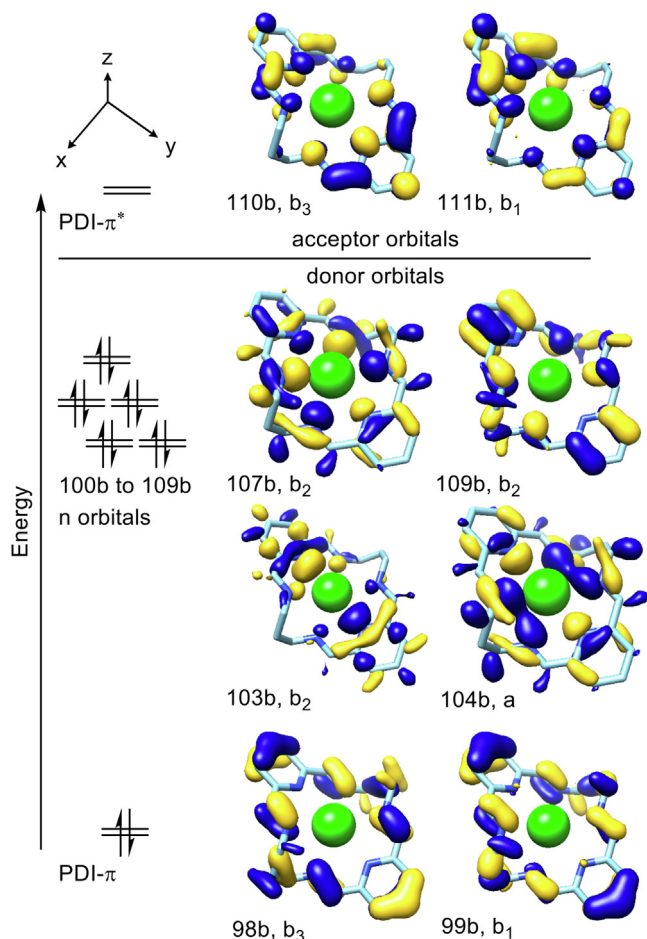


Fig. 10. DFT-calculated molecular orbitals for $[\text{}^3\text{PDAl}_2\text{Sr}]^{2+}$ involved in UV-vis electron absorption spectra with select orbital surface diagrams. Corresponding orbital numbers are noted for each calculated orbital along with an assigned Mulliken symmetry designation based upon an idealized D_2 symmetry.

components are experiencing a change in absolute energy as a function of the substitution on the imine carbon. However, the cathodic features observed by CV are well known to correspond to reduction of the ligand π^* manifold. The varying $E_{1/2}$ values for

Reduction 1 indicate that the substitution on the imine carbon is influencing the absolute energy of the ligand π^* manifold. This implies that the ligand-based σ -donors are largely unsusceptible to the identity of the R group on the imine carbon, at least within the limited range of examples studied herein. It is further worth noting that the $n \rightarrow \pi^*$ transitions do not change based on the identity of the metal in the complex, indicating that the energy of the metal-nitrogen based σ -orbitals are relatively insensitive to the changes in Lewis acidity of the template ion.

The higher energy features experimentally observed at *ca.* 40,000 cm^{-1} (250 nm) are modeled as $\pi \rightarrow \pi^*$ transitions, where the ground state π orbitals contain a significant contribution of imine π character and the excited state orbitals are the aforementioned linear combinations of the a_2 -PD(A) I_{π^*} and b_1 -PD(A) I_{π^*} fragments (Fig. 10). We find it reasonable that these $\pi \rightarrow \pi^*$ transitions would be less sensitive to the substitution at the imine carbon as both the imine π and imine π^* contributions to the respective PD(A) I_{π} and PD(A) I_{π^*} orbitals would be similarly affected by the change in the substitution at the imine carbon.

3. Conclusions

A series of macrocyclic ligands with pocket sizes of 18, 20 and 22 atoms have been synthesized via [2 + 2] Schiff base condensation reactions using alkaline earth metal template ions. The enhanced solubility imparted by the installation of a *tert*-butyl group on the 4-positions of pyridyl rings dramatically improves product yields and allows for characterization of the macrocycles by NMR spectroscopy, mass spectrometry, UV-Vis spectroscopy, cyclic voltammetry and single crystal X-ray crystallography. The use of triflate anions also allowed for multi-gram scale reactions to be conducted more safely than earlier iterations of this chemistry which used perchlorate salts. The inherent flexibility of the macrocycles imparted by the alkyl linkers offers latitude in the size of the template ion, allowing for the replacement of the more toxic barium salts with the less toxic, but smaller, alternatives of calcium and strontium [49]. Only with formation of the largest $^4\text{H}[\text{M}]$ macrocycles did template ion size seem to influence product outcomes, with significantly higher yields observed when using the largest barium ion and no product observed when using the smallest calcium ion. The redox activity of these neutral macrocyclic ligands was measured by cyclic voltammetry and square wave voltammetry, with the ability to observe the addition of four electrons into the ligand. The more cathodic reduction potentials observed for the $^{\text{nMe}}[\text{M}]$ macrocycles compared to the $^{\text{nH}}[\text{M}]$ macrocycles are indicative of changes in the energy of the $^{\text{n}}\text{PD}(\text{A}) I_2 \pi^*$ orbital. This change in energy of the imine π^* orbital can also be observed in the shift of the lower-energy UV transitions, which were attributed by way of TD-DFT calculations to ligand $n \rightarrow \pi^*$ transitions. Overall, the information provided here demonstrates how modifications to the macrocycle starting materials can be exploited toward not only improving the synthesis and solubility of the macrocycles but also tuning the electronic properties of the redox-active ligand.

4. Material and methods

4.1. General

All solvents were purchased from Fisher Scientific™. All deuterated solvents were purchased from Cambridge Isotope Laboratories, Inc. 1,4-diaminobutane, 1,3-diaminopropane, ethylenediamine and 2,6-pyridinedicarboxylic acid were purchased from Acros Organics™. Sodium peroxydisulfate, trimethylacetic acid, sodium ethoxide and selenium dioxide were

purchased from Alfa Aesar™. Silver nitrate was purchased from Strem Chemicals, Inc. Ethyl acetate was dried by stirring over calcium hydride for 24 h followed by distillation under N_2 . All other solvents and reagents were used as supplied. Dimethylpyridine-2,6-dicarboxylate was prepared according to literature procedures [74]. $\text{Ca}(\text{OTf})_2$, $\text{Sr}(\text{OTf})_2$ and $\text{Ba}(\text{OTf})_2$ were synthesized by mixing triflic acid with an excess of MCO_3 in deionized water (see SI section I for details). $(^2\text{PDI}_2)\text{Sr}(\text{OTf})_2$ and $(^3\text{PDI}_2)\text{Sr}(\text{OTf})_2$ were prepared using a modification of a previously reported procedure [26]. C, H, N Elemental analyses were performed on a Costech ECS 4010 analyzer in the Earth & Environmental Science Department at the University of Pennsylvania. ^1H , $^{13}\text{C}\{^1\text{H}\}$, HSQC, and $^{19}\text{F}\{^1\text{H}\}$ NMR spectra were recorded on a Bruker NEO 400 spectrometer. All chemical shifts (δ) are reported in units of ppm and proton and carbon chemical shifts are referenced to the residual protio-solvent signals. ^{19}F chemical shifts are referenced to external CFCl_3 standards. Infrared spectra were collected of powdered samples on an ATR plate and recorded using a Perkin-Elmer Spectrum Two FT-IR spectrometer. Nominal mass accuracy MS data were obtained by use of a Waters Acquity UPLC system equipped with a Waters TUV detector (254 nm) and a Waters SQD single quadrupole mass analyzer with electrospray ionization. Samples were detected by direct injection into the detector, bypassing the LC column, in an eluent of 99.9:0.1 v/v acetonitrile:formic acid at a flow rate of 500 $\mu\text{L}/\text{min}$; data collection 30 s.

4.2. Electrochemistry

Cyclic voltammetry and Square Wave voltammetry experiments were conducted using a BASi Epsilon E2 potentiostat. Data processing was conducted with BASi Epsilon-EC software version 2.13.77. The electrochemical cell consisted of a glassy carbon (3 mm outer diameter) working electrode, a platinum wire counter electrode and a Ag/AgCl pseudo-reference electrode. Potentials are reported versus the ferrocene/ferrocenium couple, which was added as an internal standard for reference at the end of each experiment.

4.3. UV-Vis absorption spectroscopy

UV-Vis-NIR spectra were collected on an Agilent Cary 60 UV-Vis spectrophotometer at room temperature between the wavelengths of 200 and 1000 nm and using a 1 cm path length quartz cuvette. Stock solutions for each complex were prepared, and subsequently diluted, to provide a series of measurements in the concentration range of 10 to 150 $\mu\text{mol}/\text{L}$. The absorption intensities for peak maxima were plotted vs. concentration to confirm measurements were conducted within a linear-response range of the instrument.

4.4. X-ray crystallography

X-ray intensity data were collected on a Bruker D8Quest ($^3\text{Me}[\text{Ba}]$, $^2\text{H}[\text{Sr}]$, $^3\text{H}[\text{Ca}]$, $^4\text{H}[\text{Ba}]$), a Bruker APEXII ($^2\text{Me}[\text{Ca}]$, $^2\text{Me}[\text{Sr}]$, $^3\text{Me}[\text{Sr}]$, $^2\text{H}[\text{Ca}]$, $^3\text{H}[\text{Sr}]$, $^3\text{H}[\text{Ba}]$), or a Rigaku XtaLAB Synergy-S ($^3\text{Me}[\text{Ca}]$, $^4\text{H}[\text{Sr}]$) instrument. The Bruker data were integrated with SAINT [75]; the Rigaku data were integrated using CrysAlisPro [76]. Both software packages produced a listing of unaveraged F^2 and $\sigma(F^2)$ values. All data were collected at a temperature of 100 K using Mo-K α radiation ($\lambda = 0.71073 \text{ \AA}$). The structures were solved using SHELXS-97 ($^3\text{Me}[\text{Sr}]$, $^3\text{H}[\text{Sr}]$, $^3\text{H}[\text{Ba}]$) and SHELXT ($^2\text{Me}[\text{Ca}]$, $^2\text{Me}[\text{Sr}]$, $^3\text{Me}[\text{Ca}]$, $^3\text{Me}[\text{Ba}]$, $^2\text{H}[\text{Ca}]$, $^2\text{H}[\text{Sr}]$, $^3\text{H}[\text{Ca}]$, $^4\text{H}[\text{Sr}]$, $^4\text{H}[\text{Ba}]$). All structures were refined using SHELXL [77]. The placement of hydrogen atoms was defined based upon calculated positions with respect to the parent atoms using a riding model and thermal parameters were refined isotropically. The thermal parameters for all non-

hydrogen atoms were refined anisotropically. Detailed structural and collection data is available in the SI for each complex.

4.5. DFT calculations

The density functional theory (DFT) computational studies were completed using ORCA v3.0.3 [78]. Geometry optimizations were completed using the B97-D3 level of theory [79–81] starting with truncated versions of crystallographically determined structures. Nitrogen and strontium atoms used the def2-TZVP basis sets and def2-TZVP/J auxiliary basis sets while carbon and hydrogen atoms were defined using the def2-SV(P) and def2-SV/J auxiliary basis sets [82–84]. The COSMO solvation model (conductor-like screening model) was employed using the dielectric constant of acetonitrile. SCF calculations were conducted using tight convergence limits of $1 \times 10^{-7} E_h$ in the density change, $1 \times 10^{-8} E_h$ in energy and 5×10^{-7} in the maximum element of the DIIS error vector. Molecular geometries were deemed converged once energy changes were less than $5 \times 10^{-6} E_h$, the gradient norm was smaller than $3 \times 10^{-4} E_h \text{ Bohr}^{-1}$, maximum gradient element was smaller than $1 \times 10^{-4} E_h \text{ Bohr}^{-1}$ and the maximum displacements of all atoms was less than $4 \times 10^{-3} \text{ Bohr}$ with a root-mean square of less than 2×10^{-3} . Plots of the orbitals were obtained using the Chimera software v. 1.13.1 [85]. The isosurface cutoffs in the orbital plots were set to $\pm 0.03 \text{ au}$. TD-DFT calculations were performed using the same B97-D3 functional and basis sets used for geometry optimization.

4.6. Synthesis of dimethyl 4-tert-butylpyridine-2,6-dicarboxylate (**1a**)

Dimethylpyridine-2,6-dicarboxylate (33.5 g, 0.17 mol), trimethylacetic acid (87.8 g, 0.86 mol), sodium peroxydisulfate, $\text{Na}_2\text{S}_2\text{O}_8$, (143.4 g, 0.60 mol) and silver nitrate (4.67 g, 0.027 mol) were charged to a 2000 mL round bottom flask. 1100 mL deionized water (sparged with N_2 for 15 min to remove dissolved oxygen) and 150 mL chlorobenzene were added, and the mixture was stirred vigorously under a flow of N_2 . Concentrated sulfuric acid (14 mL) was slowly added to the reaction mixture. The N_2 flow was stopped, the mixture was brought to reflux under the residual N_2 blanket (100–110 °C) and stirred for 6 h in the dark. Following the reflux period, the reaction was cooled to room temperature and approximately 250 mL saturated $\text{Na}_2\text{CO}_3(\text{aq})$ was added to the flask in small aliquots, allowing foaming to subside between additions. Additional aliquots of solid Na_2CO_3 were added until the aqueous phase reached a pH of 8. Finally, approximately 100 mL saturated $\text{NaCl}(\text{aq})$ was added to the reaction mixture to aid in the precipitation of the silver ions from solution. The reaction mixture was filtered through a pad of Celite, and the aqueous portion was extracted with $3 \times 200 \text{ mL}$ ethyl acetate. All organic layers were combined, washed with brine, and dried over Na_2SO_4 . All volatile materials were removed under reduced pressure, employing trituration with hexanes to afford a brown solid. Recrystallization from approximately 200 mL diethyl ether at $-20 \text{ }^\circ\text{C}$ for 24 h, followed by a single wash with 20 mL of cold ether afforded **1** as a white crystalline solid (29.5 g, 68 %). MP 103 °C. IR (ATR): $\nu = 1743 \text{ (C=O stretch)} \text{ cm}^{-1}$. $^1\text{H NMR}$ (400 MHz, CDCl_3 , 25 °C): $\delta = 8.29 \text{ (s, 2H, ArH)}$, 4.00 (s, 6H, OCH_3), 1.37 (s, 9H, $\text{C}(\text{CH}_3)_3$) ppm. $^{13}\text{C}\{^1\text{H}\}$ NMR (101 MHz, CDCl_3 , 25 °C): $\delta = 165.6 \text{ (s, } C_{\text{ester}})$, 163.4 (s, ArC), 148.3 (s, ArC), 125.3 (s, ArCH), 53.3 (s, OCH_3), 35.5 (s, $\text{C}(\text{CH}_3)_3$), 30.5 (s, $\text{C}(\text{CH}_3)_3$) ppm. ESI-MS: 252.4 m/z [$\text{M} + \text{H}$] $^+$, 274.4 m/z [$\text{M} + \text{Na}$] $^+$, 525.6 m/z [$2 \text{ M} + \text{Na}$] $^+$.

4.7. Alternative synthesis of dimethyl 4-tert-butylpyridine-2,6-dicarboxylate (**1b**)

Dimethylpyridine-2,6-dicarboxylate (30.7 g, 0.16 mol) and 1600 mL deionized water (sparged with N_2 for 15 min) were

charged to a 3000 mL round bottom flask. Concentrated sulfuric acid (14 mL) was slowly added, and the reaction mixture was allowed to stir for 15 min under a flow of N_2 . Trimethylacetic acid (48.4 g, 0.47 mol), silver nitrate (2.70 g, 0.016 mol) and sodium peroxydisulfate (112.9 g, 0.47 mol) were added to the flask in order. The flask was fitted with a stopper with a vent needle and the mixture was stirred at room temperature for 18 h in the dark under the residual N_2 blanket. Following the stirring period, ethyl acetate (200 mL) was added to the flask, and powdered K_2CO_3 was added in aliquots, allowing the foaming to subside after each addition, until the aqueous phase reached a pH of 8–9. Finally, approximately 100 mL saturated $\text{NaCl}(\text{aq})$ was added to the reaction mixture to help precipitate the silver ions from solution. The reaction mixture was filtered through a pad of Celite, and the aqueous portion was extracted with $3 \times 300 \text{ mL}$ ethyl acetate. All organic layers were combined, washed with brine, and dried over Na_2SO_4 . All volatile materials were removed under reduced pressure to afford an off-white solid. Recrystallization from approximately 200 mL diethyl ether at $-35 \text{ }^\circ\text{C}$ for 48 h followed by a single wash with 20 mL of cold ether afforded **1** as a white crystalline solid. Concentration of the mother liquor followed by another 48 h at $-35 \text{ }^\circ\text{C}$ afforded a second crop of crystals (28.7 g, 73 %).

4.8. Synthesis of dimethyl 4-tert-butyl-2,6-diacetylpyridine (**2**)

Compound **1** (31.2 g, 0.12 mol) and sodium ethoxide (51.1 g, 0.75 mol) were loaded to a 1000 mL round bottom flask in an N_2 atmosphere drybox. Using standard Schlenk line procedures, 250 mL of dried ethyl acetate was added to the reaction flask, and the resulting red solution was mixed under N_2 at room temperature for 40 min. An additional 300 mL of dried ethyl acetate was added to the reaction flask and the mixture was refluxed (95 °C at the Schlenk line pressure) under N_2 for 6 h. The mixture was cooled to below 75 °C and then disconnected from the Schlenk line. Concentrated hydrochloric acid (120 mL) was added in aliquots, allowing bubbling to subside after each addition, then refluxed under air for 18 h. At the end of the reflux time, the mixture was cooled to room temperature and 100 mL deionized water was added to dissolve the formed salts. Approximately 300 mL saturated $\text{Na}_2\text{CO}_3(\text{aq})$ was added to the reaction mixture in aliquots, allowing the foaming to subside at the end of each addition. Finally solid Na_2CO_3 was added to the reaction mixture until the aqueous layer reached a pH of 8. The organic layer was separated, and the aqueous layer was extracted with $3 \times 200 \text{ mL}$ ethyl acetate. All organic layers were combined, washed with brine and then dried over Na_2SO_4 . All volatile materials were removed under reduced pressure to afford a viscous red oil. Two crystallizations from approximately 100 mL hexanes at $-20 \text{ }^\circ\text{C}$ for 24 h, followed by a wash with 20 mL cold hexanes, afforded **2** as a white crystalline solid (19.6 g, 72 %). MP 52.3 °C. IR (ATR): $\nu = 1696 \text{ (C=O stretch)} \text{ cm}^{-1}$. $^1\text{H NMR}$ (400 MHz, CDCl_3 , 25 °C): $\delta = 8.20 \text{ (s, 2H, ArH)}$, 2.76 (s, 6H, CH_3), 1.34 (s, 9H, $\text{C}(\text{CH}_3)_3$) ppm. $^{13}\text{C}\{^1\text{H}\}$ NMR (101 MHz, CDCl_3 , 25 °C): $\delta = 200.1 \text{ (s, } C_{\text{ester}})$, 162.8 (s, ArC), 152.9 (s, ArC), 121.9 (s, ArCH), 35.5 (s, $\text{C}(\text{CH}_3)_3$), 30.6 (s, $\text{C}(\text{CH}_3)_3$), 25.8 (s, CH_3) ppm. ESI-MS 220.4 m/z [$\text{M} + \text{H}$] $^+$, 242.4 m/z [$\text{M} + \text{Na}$] $^+$, 283.4 m/z [$\text{M} + \text{Na}(\text{CH}_3\text{CN})$] $^+$.

4.9. Synthesis of (4-tert-butylpyridine-2,6-diyl)dimethanol (**3**)

Compound **1** (23.1 g, 0.09 mol) and 1000 mL of ethanol were loaded to a 2000 mL round bottom flask and cooled to 0 °C in an ice bath. NaBH_4 (14.1 g, 0.37 mol) was added in small aliquots over 30 min, then the ice bath was removed and the mixture was stirred at room temperature for 2 h, followed by refluxing for 12 h. The resulting red-brown solution was filtered through a pad of Celite. All volatile materials were removed under reduced pressure, and

the resulting solid was dissolved in 500 mL acetone and refluxed for 1 h. The volatile materials were again removed under reduced pressure to afford a white solid which was subsequently dissolved with 1100 mL saturated $\text{Na}_2\text{CO}_3(\text{aq})$ forming a biphasic mixture of an aqueous layer on the bottom and a red oil on the top. Additional solid Na_2CO_3 was added until the aqueous layer was again saturated. This mixture was refluxed for 1 h, then cooled to room temperature. The organic layer was separated, and the aqueous layer extracted with 3×100 mL of ethyl acetate. All organic layers were combined, washed with brine, then dried over Na_2SO_4 . All volatile materials were removed under reduced pressure and the product was crystallized from 200 mL diethyl ether at -20 °C to afford **3** as a light tan solid (12.3 g, 69 %). MP 111 °C. IR (ATR): $\nu = 3349$ (OH stretch) cm^{-1} . ^1H NMR (400 MHz, CDCl_3 , 25 °C): $\delta = 7.17$ (s, 2H, ArH), 4.75 (s, 4H, CH_2), 3.48 (br s, 2H, OH), 1.31 (s, 9H, C(CH_3)₃) ppm. $^{13}\text{C}\{^1\text{H}\}$ NMR (101 MHz, CDCl_3 , 25 °C): $\delta = 162.1$ (s, ArC), 158.4 (s, ArC), 116.5 (s, ArCH), 64.7 (s, CH_2), 35.1 (s, C(CH_3)₃), 30.7 (s, C(CH_3)₃) ppm. ESI-MS 196.4 m/z [M + H]⁺, 218.4 m/z [M + Na]⁺.

4.10. Synthesis of 4-tert-butylpyridine-2,6-dicarbaldehyde (**4**)

Compound **3** (19.8 g, 0.10 mol), selenium dioxide (11.6 g, 0.10 mol) and 550 mL of dioxane were loaded to a 1000 mL round bottom flask. The reaction mixture was refluxed for 5 h, cooled to room temp and filtered through a pad of Celite to produce a red-brown solution. All volatile materials were removed under reduced pressure, employing trituration with hexanes to remove residual dioxane until a red-brown solid formed. The product was extracted using approximately 200 mL hexanes. Two crystallizations from 100 mL hexanes at -20 °C afforded **4** as a light tan crystalline material (12.7 g, 65 %). MP 48.1 °C. IR (ATR): $\nu = 1708$ (C=O stretch) cm^{-1} . ^1H NMR (400 MHz, CDCl_3 , 25 °C): $\delta = 10.12$ (s, 2H, H_{aldimine}), 8.13 (s, 2H, ArH), 1.36 (s, 9H, C(CH_3)₃) ppm. $^{13}\text{C}\{^1\text{H}\}$ NMR (101 MHz, CDCl_3 , 25 °C): $\delta = 192.9$ (s, 2H, C_{aldimine}), 163.5 (s, ArC), 153.2 (s, ArC), 122.5 (s, ArCH), 35.6 (s, C(CH_3)₃), 30.5 (s, C(CH_3)₃) ppm. ESI-MS 192.3 m/z [M + H]⁺.

4.11. Synthesis of $(^2\text{PDI}_2)\text{Ca}(\text{OTf})_2$ ($^{2\text{Me}}[\text{Ca}]$)

A solution of $\text{Ca}(\text{OTf})_2$ (1.85 g, 5.5 mmol) and **2** (2.40 g, 10.9 mmol) in 150 mL of methanol was stirred at room temperature for 15 min. Ethylenediamine (0.67 g, 11.1 mmol) was added, and the resulting yellow solution was then refluxed for 12 h. After cooling the reaction mixture to room temperature, all volatile materials were then removed under reduced pressure. The off-white solid was dissolved in approximately 15 mL of dichloromethane, filtered through a plug of Celite and layered with 50 mL of hexanes. Storing this layered sample at -20 °C for 48 h afforded compound $^{2\text{Me}}[\text{Ca}]$ as an off-white microcrystalline solid (4.25 g, 95 % yield). Colorless block crystals suitable for single crystal X-ray crystallography were grown at room temperature from a solution of $^{2\text{Me}}[\text{Ca}]$ in chloroform layered with diethyl ether. MP decomp. > 220 °C. Anal. Calcd. for $\text{C}_{32}\text{H}_{42}\text{CaF}_6\text{N}_6\text{O}_6\text{S}_2$ (824.91 g/mol): C, 46.59; H, 5.13; N, 10.19. Found: C, 46.46; H, 5.40; N, 9.85%. UV-Vis $\lambda_{\text{max}}(\text{THF})/\text{nm}$ ($\epsilon/\text{M}^{-1} \text{cm}^{-1}$): 292 (9800), 245 (30100). UV-Vis $\lambda_{\text{max}}(\text{DCM})/\text{nm}$ ($\epsilon/\text{M}^{-1} \text{cm}^{-1}$): 294 (9000), 245 (32700). IR (ATR): $\nu = 1603(\text{s}), 1647(\text{s})$ (C=N stretch) cm^{-1} . ^1H NMR (400 MHz, CDCl_3 , 25 °C): $\delta = 7.76$ (s, 4H, ArH), 3.92 (s, 8H, NCH_2), 2.44 (s, 12H, CH_3), 1.39 (s, 18H, C(CH_3)₃) ppm. $^{13}\text{C}\{^1\text{H}\}$ NMR (101 MHz, CDCl_3 , 25 °C): $\delta = 167.0$ (s, C_{imine}), 164.4 (s, ArC), 154.3 (s, ArC), 119.9 (d (2 CF_3 peaks missing), $^1J_{\text{FC}} = 320.2$ Hz, CF_3), 120.6 (s, ArCH), 52.1 (s, NCH_2), 35.5 (s, C(CH_3)₃), 30.6 (s, C(CH_3)₃), 15.8 (s, CH_3) ppm. $^{19}\text{F}\{^1\text{H}\}$ NMR (376 MHz, CDCl_3 , 25 °C): $\delta = -78.9$ (s, CF_3) ppm. ESI-MS 675.7 m/z [$(^2\text{PDI}_2)\text{Ca}(\text{OTf})$]⁺.

4.12. Synthesis of $(^2\text{PDI}_2)\text{Sr}(\text{OTf})_2$ ($^{2\text{Me}}[\text{Sr}]$)

This is a modification to a procedure reported previously by our group [26]. A solution of $\text{Sr}(\text{OTf})_2$ (2.84 g, 7.36 mmol) and **2** (3.23 g, 14.7 mmol) in 300 mL of methanol was stirred at room temperature for 15 min. Ethylenediamine (0.90 g, 15.0 mmol) was added, and the resulting yellow solution was refluxed for 12 h. After cooling the reaction mixture to room temperature, all volatile materials were removed under reduced pressure. The off-white solid was dissolved in approximately 20 mL of dichloromethane, filtered through a plug of Celite and layered with 90 mL of hexanes. Storing this layered sample at 20 °C for 48 h afforded $^{2\text{Me}}[\text{Sr}]$ as an off-white microcrystalline solid (5.89 g, 92 % yield). Colorless block crystals suitable for single crystal X-ray crystallography were grown at room temperature from vapor diffusion of pentane into a solution of $^{2\text{Me}}[\text{Sr}]$ in fluorobenzene. MP decomp. > 220 °C. Anal. Calcd. for $\text{C}_{32}\text{H}_{42}\text{F}_6\text{N}_6\text{O}_6\text{S}_2\text{Sr}$ (872.45 g/mol): C, 44.05; H, 4.85; N, 9.63. Found: C, 44.43, H, 5.03, N, 9.66%. UV-Vis $\lambda_{\text{max}}(\text{THF})/\text{nm}$ ($\epsilon/\text{M}^{-1} \text{cm}^{-1}$): 291 (11200), 247 (32900). UV-Vis $\lambda_{\text{max}}(\text{DCM})/\text{nm}$ ($\epsilon/\text{M}^{-1} \text{cm}^{-1}$): 293 (10600), 245 (36900). IR (ATR): $\nu = 1601(\text{s}), 1642(\text{s})$ (C=N stretch) cm^{-1} . ^1H NMR (400 MHz, CDCl_3 , 25 °C): $\delta = 7.78$ (s, 4H, ArH), 3.91 (s, 8H, NCH_2), 2.46 (s, 12H, CH_3), 1.41 (s, C(CH_3)₃) ppm. $^{13}\text{C}\{^1\text{H}\}$ NMR (101 MHz, CDCl_3 , 25 °C): $\delta = 167.8$ (s, C_{imine}), 164.1 (s, ArC), 155.6 (s, ArC), 121.2 (s, ArCH), 120.1 (d (2 CF_3 peaks missing), $^1J_{\text{FC}} = 321.2$ Hz, CF_3), 52.6 (s, NCH_2), 35.5 (s, C(CH_3)₃), 30.6 (s, C(CH_3)₃), 16.4 (s, CH_3) ppm. $^{19}\text{F}\{^1\text{H}\}$ NMR (376 MHz, CDCl_3 , 25 °C): $\delta = -78.8$ (s, CF_3) ppm. ESI-MS 723.6 m/z [$(^2\text{PDI}_2)\text{Sr}(\text{OTf})$]⁺.

4.13. Synthesis of $(^3\text{PDI}_2)\text{Ca}(\text{OTf})_2$ ($^{3\text{Me}}[\text{Ca}]$)

A solution of $\text{Ca}(\text{OTf})_2$ (0.418 g, 1.24 mmol) and **2** (0.542 g, 2.47 mmol) in 50 mL of methanol was stirred at room temperature for 15 min. 1,3-diaminopropane (0.198 g, 2.67 mmol) was added, and the resulting yellow solution was then refluxed for 20 h. After cooling the reaction mixture to room temperature, all volatile materials were removed under reduced pressure. The solid was dissolved in approximately 10 mL of dichloromethane, filtered through a plug of Celite, and layered with 30 mL of hexanes. Storing this layered sample at -20 °C for 48 h afforded compound $^{3\text{Me}}[\text{Ca}]$ as an off-white microcrystalline solid (0.979 g, 93 % yield). Colorless block crystals suitable for single crystal X-ray crystallography were grown at room temperature from vapor diffusion of diethyl ether into a solution of $^{3\text{Me}}[\text{Ca}]$ in methanol. MP decomp. > 220 °C. Anal. Calcd. for $\text{C}_{34}\text{H}_{46}\text{CaF}_6\text{N}_6\text{O}_6\text{S}_2$ (852.97 g/mol): C, 47.88; H, 5.44; N, 9.85. Found: C, 48.01; H, 5.44; N, 9.85%. UV-Vis $\lambda_{\text{max}}(\text{THF})/\text{nm}$ ($\epsilon/\text{M}^{-1} \text{cm}^{-1}$): 296 (10000), 246 (32000). UV-Vis $\lambda_{\text{max}}(\text{DCM})/\text{nm}$ ($\epsilon/\text{M}^{-1} \text{cm}^{-1}$): 296 (9100), 242 (32000). IR (ATR): $\nu = 1603(\text{s}), 1655(\text{s})$ (C=N stretch) cm^{-1} . ^1H NMR (400 MHz, CDCl_3 , 25 °C): $\delta = 7.82$ (s, 4H, ArH), 3.87 (br s, 8H, NCH_2), 2.45 (s, 12H, CH_3), 1.83 (m, 4H, CH_2), 1.44 (s, 18H, C(CH_3)₃) ppm. $^{13}\text{C}\{^1\text{H}\}$ NMR (101 MHz, CDCl_3 , 25 °C): $\delta = 165.6$ (s, C_{imine}), 164.4 (s, ArC), 154.9 (s, ArC), 121.1 (s, ArCH), 120.1 (d, (2 CF_3 peaks missing), $^1J_{\text{FC}} = 320.2$ Hz, CF_3), 46.6 (s, NCH_2), 35.6 (s, C(CH_3)₃), 30.6 (s, C(CH_3)₃), 28.6 (s, CH_2), 14.7 (s, CH_3) ppm. $^{19}\text{F}\{^1\text{H}\}$ NMR (376 MHz, CDCl_3 , 25 °C): $\delta = -78.8$ (s, CF_3) ppm. ESI-MS 703.7 m/z [$(^3\text{PDI}_2)\text{Ca}(\text{OTf})$]⁺.

4.14. Synthesis of $(^3\text{PDI}_2)\text{Sr}(\text{OTf})_2$ ($^{3\text{Me}}[\text{Sr}]$)

This is a modification to a procedure reported previously by our group [26]. A solution of $\text{Sr}(\text{OTf})_2$ (3.73 g, 9.66 mmol) and **2** (4.24 g, 19.3 mmol) in 400 mL of methanol was stirred at room temperature for 15 min. 1,3-diaminopropane (1.44 g, 19.4 mmol) was added, and the resulting yellow solution was then refluxed for 18 h. After cooling the reaction mixture to room temperature, all volatile

materials were then removed under reduced pressure. The solid was dissolved in approximately 25 mL of dichloromethane and layered with 75 mL of hexanes. Storing this layered sample at $-20\text{ }^{\circ}\text{C}$ for 48 h afforded compound ${}^3\text{Me}[\text{Sr}]$ as an off-white microcrystalline solid (8.06 g, 93 % yield). Colorless block crystals suitable for single crystal X-ray crystallography were grown at room temperature from a solution of ${}^3\text{Me}[\text{Sr}]$ in THF layered with hexane. MP decomp. $> 220\text{ }^{\circ}\text{C}$. Anal. Calcd. for $\text{C}_{34}\text{H}_{46}\text{F}_6\text{N}_6\text{O}_6\text{S}_2\text{Sr}$ (900.51 g/mol): C, 45.35; H, 5.15; N, 9.33. Found: C, 45.73; H, 5.13; N, 9.00%. UV-Vis $\lambda_{\text{max}}(\text{THF})/\text{nm}$ ($\epsilon/\text{M}^{-1}\text{ cm}^{-1}$): 294 (6800), 244 (32000). UV-Vis $\lambda_{\text{max}}(\text{DCM})/\text{nm}$ ($\epsilon/\text{M}^{-1}\text{ cm}^{-1}$): 293 (9300), 243 (32700). IR (ATR): $\nu = 1602(\text{s}), 1644(\text{s})$ (C=N stretch) cm^{-1} . ${}^1\text{H}$ NMR (400 MHz, CDCl_3 , $25\text{ }^{\circ}\text{C}$): $\delta = 7.81$ (s, 4H, ArH), 3.96 (t, ${}^3J_{\text{HH}} = 6$ Hz, 8H, NCH_2), 2.46 (s, 12H, CH_3), 1.89 (quint, ${}^3J_{\text{HH}} = 6$ Hz, 4H, CH_2), 1.42 (s, 18H, $\text{C}(\text{CH}_3)_3$) ppm. ${}^{13}\text{C}\{^1\text{H}\}$ NMR (101 MHz, CDCl_3 , $25\text{ }^{\circ}\text{C}$): $\delta = 167.1$ (s, C_{imine}), 164.0 (s, ArC), 155.5 (s, ArC), 121.4 (s, ArCH), 120.0 (d, (2 CF_3 peaks missing)) ${}^1J_{\text{FC}} = 299.0$ Hz, CF_3), 46.7 (s, NCH_2), 35.5 (s, $\text{C}(\text{CH}_3)_3$), 30.7 (s, $\text{C}(\text{CH}_3)_3$), 28.9 (s, CH_2), 15.3 (s, CH_3) ppm. ${}^{19}\text{F}\{^1\text{H}\}$ NMR (376 MHz, CDCl_3 , $25\text{ }^{\circ}\text{C}$): $\delta = -78.7$ (s, CF_3) ppm. ESI-MS 751.8 m/z [${}^3\text{PDI}_2$] $\text{Sr}(\text{OTf})_2^+$.

4.15. Synthesis of $({}^3\text{PDI}_2)\text{Ba}(\text{OTf})_2$ (${}^3\text{Me}[\text{Ba}]$)

A solution of $\text{Ba}(\text{OTf})_2$ (2.28 g, 4.7 mmol) and **2** (2.00 g, 9.4 mmol) in 200 mL of methanol was stirred at room temperature for 15 min. 1,3-diaminopropane (0.77 g, 9.3 mmol) was added, and the resulting yellow solution was then refluxed for 12 h. After cooling the reaction mixture to room temperature, all volatile materials were then removed under reduced pressure. The solid was dissolved in approximately 40 mL of chloroform and layered with 40 mL of hexanes. Storing this layered sample at $-20\text{ }^{\circ}\text{C}$ for 48 h afforded compound ${}^3\text{Me}[\text{Ba}]$ as an off-white microcrystalline solid (3.42 g, 70 % yield). Colorless block crystals suitable for single crystal X-ray crystallography were grown at room temperature from a solution of ${}^3\text{Me}[\text{Ba}]$ in chloroform layered with toluene. MP decomp. $> 220\text{ }^{\circ}\text{C}$. Anal. Calcd. for $\text{C}_{34}\text{H}_{46}\text{BaF}_6\text{N}_6\text{O}_6\text{S}_2$ (950.21 g/mol): C, 42.98; H, 4.88; N, 8.84. Found: C, 42.91; H, 5.01; N, 8.83%. UV-Vis $\lambda_{\text{max}}(\text{THF})/\text{nm}$ ($\epsilon/\text{M}^{-1}\text{ cm}^{-1}$): 286 (7600), 243 (22400). UV-Vis $\lambda_{\text{max}}(\text{DCM})/\text{nm}$ ($\epsilon/\text{M}^{-1}\text{ cm}^{-1}$): 289 (7000), 243 (22900). IR (ATR): $\nu = 1597(\text{s})$ (C=N stretch) cm^{-1} . ${}^1\text{H}$ NMR (400 MHz, CDCl_3 , $25\text{ }^{\circ}\text{C}$): $\delta = 7.75$ (s, 4H, ArH), 3.93 (t, ${}^3J_{\text{HH}} = 6$ Hz, 8H, NCH_2), 2.43 (s, 12H, CH_3), 2.06 (quint, ${}^3J_{\text{HH}} = 6$ Hz, 4H, CH_2), 1.40 (s, 18H, $\text{C}(\text{CH}_3)_3$) ppm. ${}^{13}\text{C}\{^1\text{H}\}$ NMR (101 MHz, CDCl_3 , $25\text{ }^{\circ}\text{C}$): $\delta = 167.1$ (s, C_{imine}), 163.7 (s, ArC), 156.5 (s, ArC), 121.6 (s, ArCH), 120.2 (q, ${}^1J_{\text{FC}} = 320.7$ Hz, CF_3), 47.7 (s, NCH_2), 35.5 (s, $\text{C}(\text{CH}_3)_3$), 30.6 (s, $\text{C}(\text{CH}_3)_3$), 29.2 (s, CH_2), 16.3 (s, CH_3) ppm. ${}^{19}\text{F}\{^1\text{H}\}$ NMR (376 MHz, CDCl_3 , $25\text{ }^{\circ}\text{C}$): $\delta = -78.60$ (s, CF_3) ppm. ESI-MS 801.9 m/z [${}^3\text{PDI}_2$] $\text{Ba}(\text{OTf})_2^+$.

4.16. Synthesis of $({}^2\text{PDAI}_2)\text{Ca}(\text{OTf})_2$ (${}^{2\text{H}}[\text{Ca}]$)

A solution of $\text{Ca}(\text{OTf})_2$ (1.49 g, 4.4 mmol) and **4** (1.68 g, 8.8 mmol) in 150 mL of methanol was stirred at room temperature for 15 min. Ethylenediamine (0.52 g, 8.7 mmol) was added and the resulting solution was stirred at room temperature for 6 h. All volatile materials were then removed under reduced pressure and the off-white solid was washed with 20 mL of dichloromethane to isolate ${}^{2\text{H}}[\text{Ca}]$ as a white microcrystalline solid. An additional crop of product was recovered by layering the dichloromethane wash with 40 mL of hexanes, and storing this layered sample at $-20\text{ }^{\circ}\text{C}$ for 48 h (2.46 g, 69 % yield). Colorless block crystals suitable for single crystal X-ray crystallography were grown at room temperature from vapor diffusion of diethyl ether into a solution of ${}^{2\text{H}}[\text{Ca}]$ in methanol. MP decomp. $> 220\text{ }^{\circ}\text{C}$. Anal. Calcd. for $\text{C}_{28}\text{H}_{34}\text{CaF}_6\text{N}_6\text{O}_6\text{S}_2$ (768.80 g/mol): C, 43.74; H, 4.46; N, 10.93. Found: C, 43.40; H, 4.78; N, 10.67%. IR (ATR): $\nu = 1606(\text{s}), 1663(\text{s})$ (C=N stretch)

cm^{-1} . ${}^1\text{H}$ NMR (400 MHz, CD_3OD , $25\text{ }^{\circ}\text{C}$): $\delta = 8.80$ (s, 4H, N = CH), 8.07 (s, 4H, ArH), 4.07 (s, 8H, NCH_2), 1.49 (s, $\text{C}(\text{CH}_3)_3$) ppm. ${}^{13}\text{C}\{^1\text{H}\}$ NMR (101 MHz, CD_3OD , $25\text{ }^{\circ}\text{C}$): $\delta = 167.9$ (s, ArC), 164.6 (s, C_{imine}), 153.6 (s, ArC), 126.7 (s, ArCH), 121.8 (d, (2 CF_3 peaks missing)) ${}^1J_{\text{FC}} = 320.2$ Hz, CF_3), 61.1 (s, NCH_2), 36.6 (s, $\text{C}(\text{CH}_3)_3$), 30.6 (s, $\text{C}(\text{CH}_3)_3$), ppm. ${}^{19}\text{F}\{^1\text{H}\}$ NMR (376 MHz, CDCl_3 , $25\text{ }^{\circ}\text{C}$): $\delta = -80.1$ (s, CF_3) ppm. ESI-MS 619.5 m/z [${}^2\text{PDAI}_2$] $\text{Ca}(\text{OTf})_2^+$.

4.17. Synthesis of $({}^2\text{PDAI}_2)\text{Sr}(\text{OTf})_2$ (${}^{2\text{H}}[\text{Sr}]$)

A solution of $\text{Sr}(\text{OTf})_2$ (2.08 g, 5.4 mmol) and **4** (2.06 g, 0.011 mol) in 225 mL of methanol was stirred at room temperature for 15 min. Ethylenediamine (0.64 g, 0.011 mol) was added and the resulting solution was stirred at room temperature for 6 h. All volatile materials were then removed under reduced pressure and the off-white solid was washed with 20 mL cold acetonitrile ($-20\text{ }^{\circ}\text{C}$) to isolate ${}^{2\text{H}}[\text{Sr}]$ as a white microcrystalline solid (3.34 g, 76 % yield). Crystals suitable for single crystal X-ray crystallography were grown at room temperature from vapor diffusion of diethyl ether into a solution of ${}^{2\text{H}}[\text{Sr}]$ in methanol. MP decomp. $> 220\text{ }^{\circ}\text{C}$. Anal. Calcd. for $\text{C}_{32}\text{H}_{42}\text{SrF}_6\text{N}_6\text{O}_6\text{S}_2$ (816.35 g/mol): C, 41.20; H, 4.20; N, 10.29. Found: C, 41.32; H, 4.59; N, 10.26%. IR (ATR): $\nu = 1602(\text{s}), 1656(\text{s})$ (C=N stretch) cm^{-1} . ${}^1\text{H}$ NMR (400 MHz, CD_3OD , $25\text{ }^{\circ}\text{C}$): $\delta = 8.77$ (s, 4H, N = CH), 8.05 (s, 4H, ArH), 4.09 (s, 8H, NCH_2), 1.48 (s, $\text{C}(\text{CH}_3)_3$) ppm. ${}^{13}\text{C}\{^1\text{H}\}$ NMR (101 MHz, CD_3OD , $25\text{ }^{\circ}\text{C}$): $\delta = 167.4$ (s, ArC), 164.5 (s, C_{imine}), 154.4 (s, ArC), 126.7 (s, ArCH), (CF_3 peaks missing), 60.5 (s, NCH_2), 36.5 (s, $\text{C}(\text{CH}_3)_3$), 30.7 (s, $\text{C}(\text{CH}_3)_3$), ppm. ${}^{19}\text{F}\{^1\text{H}\}$ NMR (376 MHz, CDCl_3 , $25\text{ }^{\circ}\text{C}$): $\delta = -80.1$ (s, CF_3) ppm. ESI-MS 667.5 m/z [${}^2\text{PDAI}_2$] $\text{Sr}(\text{OTf})_2^+$.

4.18. Synthesis of $({}^3\text{PDAI}_2)\text{Ca}(\text{OTf})_2$ (${}^{3\text{H}}[\text{Ca}]$)

A solution of $\text{Ca}(\text{OTf})_2$ (0.419 g, 1.24 mmol) and **4** (0.474 g, 2.47 mol) in 100 mL of methanol was stirred at room temperature for 15 min. 1,3-diaminopropane (0.209 g, 2.82 mmol) was added and the resulting solution was stirred at room temperature for 7 h. All volatile materials were then removed under reduced pressure. The off-white solid was dissolved in 5 mL of methanol, filtered through Celite and layered with 15 mL of diethyl ether. After 48 h at room temperature, ${}^{3\text{H}}[\text{Ca}]$ was isolated as a white crystalline solid (0.585 g, 59 % yield). Crystals suitable for single crystal X-ray crystallography were grown at room temperature from vapor diffusion of diethyl ether into a solution of ${}^{3\text{H}}[\text{Ca}]$ in acetonitrile. MP decomp. $> 220\text{ }^{\circ}\text{C}$. Anal. Calcd. for $\text{C}_{30}\text{H}_{38}\text{F}_6\text{N}_6\text{O}_6\text{S}_2\text{Ca}$ (796.86 g/mol): C, 45.22; H, 4.81; N, 10.55. Found: C, 44.84; H, 4.84; N, 10.24%. UV-Vis $\lambda_{\text{max}}(\text{THF})/\text{nm}$ ($\epsilon/\text{M}^{-1}\text{ cm}^{-1}$): 313 (11600), 301 (18100), 290 (15400), 247 (40500). UV-Vis $\lambda_{\text{max}}(\text{DCM})/\text{nm}$ ($\epsilon/\text{M}^{-1}\text{ cm}^{-1}$): 313 (11600), 301 (18100), 290 (15400), 247 (43100). IR (ATR): $\nu = 1602(\text{s}), 1660(\text{s})$ (C=N stretch) cm^{-1} . ${}^1\text{H}$ NMR (400 MHz, CD_3OD , $25\text{ }^{\circ}\text{C}$): $\delta = 8.70$ (s, 4H, H_{imine}), 8.04 (s, 4H, ArH), 3.87 (t, ${}^3J_{\text{HH}} = 7$ Hz, 8H, NCH_2), 2.19 (quint, ${}^3J_{\text{HH}} = 7$ Hz, 4H, CH_2), 1.47 (s, 18H $\text{C}(\text{CH}_3)_3$) ppm. ${}^{13}\text{C}\{^1\text{H}\}$ NMR (101 MHz, CD_3OD , $25\text{ }^{\circ}\text{C}$): $\delta = 168.0$ (s, ArC), 164.9 (s, C_{imine}), 153.7 (s, ArC), 126.5 (s, ArCH), (CF_3 peaks missing), 55.1 (s, NCH_2), 36.6 (s, $\text{C}(\text{CH}_3)_3$), 31.0 (s, $\text{C}(\text{CH}_3)_3$), 30.6 (s, CH_2) ppm. ${}^{19}\text{F}\{^1\text{H}\}$ NMR (376 MHz, CD_3OD , $25\text{ }^{\circ}\text{C}$): $\delta = -80.1$ (s, CF_3) ppm. ESI-MS 647.7 m/z [${}^3\text{PDAI}_2$] $\text{Ca}(\text{OTf})_2^+$.

4.19. Synthesis of $({}^3\text{PDAI}_2)\text{Sr}(\text{OTf})_2$ (${}^{3\text{H}}[\text{Sr}]$)

A solution of $\text{Sr}(\text{OTf})_2$ (2.25 g, 5.8 mmol) and **4** (2.23 g, 11.7 mol) in 225 mL of methanol was stirred at room temperature for 15 min. 1,3-diaminopropane (0.86 g, 11.7 mmol) was added and the resulting solution was stirred at room temperature for 4 h. All volatile materials were then removed under reduced pressure and the off-white solid was washed with cold acetonitrile ($-20\text{ }^{\circ}\text{C}$) to isolate ${}^{3\text{H}}[\text{Sr}]$ as a white microcrystalline solid (3.79 g, 77 % yield).

Crystals suitable for single crystal X-ray crystallography were grown at room temperature from vapor diffusion of diethyl ether into a solution of $^{3\text{H}}[\text{Sr}]$ in acetonitrile. MP decomp. > 220 °C. Anal. Calcd. for $\text{C}_{30}\text{H}_{38}\text{SrF}_6\text{N}_6\text{O}_6\text{S}_2$ (844.40 g/mol): C, 42.67; H, 4.54; N, 9.95. Found: C, 42.68; H, 4.86; N, 9.81%. IR (ATR): $\nu = 1600(\text{s}), 1660(\text{s})$ (C=N stretch) cm^{-1} . ^1H NMR (400 MHz, CD_3OD , 25 °C): $\delta = 8.71$ (s, 4H, H_{imine}); 8.02 (s, 4H, ArH), 3.95 (t, $^3J_{\text{HH}} = 6$ Hz, 8H, NCH_2), 2.24 (quint, $^3J_{\text{HH}} = 6$ Hz, 4H, CH_2), 1.47 (s, 18H $\text{C}(\text{CH}_3)_3$) ppm. $^{13}\text{C}\{^1\text{H}\}$ NMR (101 MHz, CD_3OD , 25 °C): $\delta = 167.2$ (s, ArC), 165.5 (s, C_{imine}), 154.1 (s, ArC), 126.8 (s, ArCH), (CF_3 peaks missing), 57.1 (s, NCH_2), 36.5 (s, $\text{C}(\text{CH}_3)_3$), 30.68 (s, CH_2), 30.65 (s, $\text{C}(\text{CH}_3)_3$) ppm. $^{19}\text{F}\{^1\text{H}\}$ NMR (376 MHz, CD_3OD , 25 °C): $\delta = -80.0$ (s, CF_3) ppm. ESI-MS 695.6 m/z [$^{3\text{H}}\text{PDAI}_2\text{Sr}(\text{OTf})$] $^+$.

4.20. Synthesis of $(^3\text{PDAI}_2)\text{Ba}(\text{OTf})_2$ ($^{3\text{H}}[\text{Ba}]$)

A solution of $\text{Ba}(\text{OTf})_2$ (2.28 g, 5.2 mmol) and **4** (2.00 g, 10.5 mol) in 200 mL of methanol was stirred at room temperature for 15 min. 1,3-diaminopropane (0.77 g, 10.4 mmol) was added and the resulting solution was stirred at room temperature for 6 h. All volatile materials were then removed under reduced pressure and the resulting white solid was dissolved in approximately 30 mL of chloroform and layered with 30 mL of hexanes. Storing this layered sample at -20 °C for 48 h afforded compound $^{3\text{H}}[\text{Ba}]$ as a white microcrystalline solid (3.42 g, 74 % yield). Crystals suitable for single crystal X-ray crystallography were grown at room temperature from vapor diffusion of diethyl ether into a solution of $^{3\text{H}}[\text{Ba}]$ in acetonitrile. MP decomp. > 220 °C. Anal. Calcd. for $\text{C}_{30}\text{H}_{38}\text{BaF}_6\text{N}_6\text{O}_6\text{S}_2$ (894.11 g/mol): C, 40.30; H, 4.28; N, 9.40. Found: C, 40.26; H, 4.54; N, 9.23%. UV-Vis $\lambda_{\text{max}}(\text{THF})/\text{nm}$ ($\epsilon/\text{M}^{-1}\text{cm}^{-1}$): 313 (8400), 302 (12300), 290 (9300), 246 (26400). UV-Vis $\lambda_{\text{max}}(\text{DCM})/\text{nm}$ ($\epsilon/\text{M}^{-1}\text{cm}^{-1}$): 315 (8100), 301 (12200), 290 (8900), 245 (27100). IR (ATR): $\nu = 1596(\text{s})$ (C=N stretch) cm^{-1} . ^1H NMR (400 MHz, CD_3OD , 25 °C): $\delta = 8.65$ (s, 4H, H_{imine}); 7.93 (s, 4H, ArH), 4.00 (t, $^3J_{\text{HH}} = 4$ Hz, 8H, NCH_2), 2.28 (br s, 4H, CH_2), 1.42 (s, 18H $\text{C}(\text{CH}_3)_3$) ppm. $^{13}\text{C}\{^1\text{H}\}$ NMR (101 MHz, CD_3OD , 25 °C): $\delta = 166.6$ (s, ArC), 166.0 (s, C_{imine}), 154.5 (s, ArC), 127.2 (s, ArCH), 121.7 (q, $^1J_{\text{FC}} = 319.8$ Hz, CF_3), 61.5 (s, NCH_2), 36.3 (s, $\text{C}(\text{CH}_3)_3$), 31.5 (s, CH_2), 30.6 (s, $\text{C}(\text{CH}_3)_3$) ppm. $^{19}\text{F}\{^1\text{H}\}$ NMR (376 MHz, CD_3OD , 25 °C): $\delta = -80.0$ (s, CF_3) ppm. ESI-MS 745.7 m/z [$^{3\text{H}}\text{PDAI}_2\text{Ba}(\text{OTf})$] $^+$.

4.21. Synthesis of $(^4\text{PDAI}_2)\text{Sr}(\text{OTf})_2$ ($^{4\text{H}}[\text{Sr}]$)

A solution of $\text{Sr}(\text{OTf})_2$ (2.43 g, 6.3 mmol) and **4** (2.11 g, 0.011 mol) in 325 mL of methanol was stirred at room temperature for 15 min. 1,4-diaminopropane (0.97 g, 0.011 mol) was added and the resulting solution was stirred at room temperature for 6 h. All volatile materials were then removed under reduced pressure and the resulting off-white glassy solid was dissolved in approximately 20 mL of chloroform, filtered through a plug of Celite and layered with 200 mL of hexanes. Storing this layered sample at -20 °C for 48 h afforded compound $^{4\text{H}}[\text{Sr}]$ as an off-white microcrystalline solid (2.46 g, 51 % yield). Crystals suitable for single crystal X-ray crystallography were grown at -20 °C from a solution of $^{4\text{H}}[\text{Sr}]$ in chloroform layered with diethyl ether. MP decomp. > 220 °C. Anal. Calcd. for $\text{C}_{32}\text{H}_{42}\text{SrF}_6\text{N}_6\text{O}_6\text{S}_2$ (872.45 g/mol): C, 44.05; H, 4.85; N, 9.63. Found: C, 43.66; H, 4.75; N, 9.27%. UV-Vis $\lambda_{\text{max}}(\text{THF})/\text{nm}$ ($\epsilon/\text{M}^{-1}\text{cm}^{-1}$): 315 (12100), 303 (16400), 292 (12100), 248 (32200). UV-Vis $\lambda_{\text{max}}(\text{DCM})/\text{nm}$ ($\epsilon/\text{M}^{-1}\text{cm}^{-1}$): 315 (12900), 303 (17400), 292 (12600), 248 (33700). IR (ATR): $\nu = 1600(\text{s})$ (C=N stretch) cm^{-1} . ^1H NMR (400 MHz, CD_3OD , 25 °C): $\delta = 8.69$ (s, 4H, H_{imine}); 8.00 (s, 4H, ArH), 3.89 (br s, 8H, NCH_2), 2.13 (br s, 8H, CH_2), 1.46 (s, 18H $\text{C}(\text{CH}_3)_3$) ppm. $^{13}\text{C}\{^1\text{H}\}$ NMR (101 MHz, CD_3OD , 25 °C): $\delta = 167.2$ (s, ArC), 165.4 (s, C_{imine}), 154.1 (s, ArC), 127.2 (s, ArCH), 121.7 (q, $^1J_{\text{FC}} = 320$ Hz, CF_3), 61.5 (s, NCH_2), 36.4 (s, $\text{C}(\text{CH}_3)_3$), 30.6 (s, $\text{C}(\text{CH}_3)_3$), 28.8 (s, CH_2) ppm. $^{19}\text{F}\{^1\text{H}\}$ NMR (376 MHz, CD_3OD , 25 °C): $\delta = -80.0$ (s, CF_3) ppm. ESI-MS 723.7 m/z [$^{4\text{H}}\text{PDAI}_2\text{Sr}(\text{OTf})$] $^+$.

4.22. Synthesis of $(^4\text{PDAI}_2)\text{Ba}(\text{OTf})_2$ ($^{4\text{H}}[\text{Ba}]$)

A solution of $\text{Ba}(\text{OTf})_2$ (2.45 g, 5.36 mmol) and **4** (2.15 g, 0.011 mol) in 325 mL of methanol was stirred at room temperature for 15 min. 1,4-diaminopropane (0.99 g, 0.011 mol) was added and the resulting solution was stirred at room temperature for 6 h. All volatile materials were then removed under reduced pressure and the resulting light purple, glassy solid was dissolved in approximately 20 mL of chloroform, filtered through a plug of Celite and layered with 200 mL of hexanes. Storing this layered sample at -20 °C for 48 h afforded compound $^{4\text{H}}[\text{Ba}]$ as an off-white microcrystalline solid (4.62 g, 89 % yield). Crystals suitable for single crystal X-ray crystallography were grown at room temperature from vapor diffusion of diethyl ether into a solution of $^{4\text{H}}[\text{Ba}]$ in acetonitrile. MP decomp. > 220 °C. Anal. Calcd. for $\text{C}_{32}\text{H}_{42}\text{BaF}_6\text{N}_6\text{O}_6\text{S}_2$ (922.16 g/mol): C, 41.68; H, 4.59; N, 9.11. Found: C, 41.36; H, 4.59; N, 8.80%. UV-Vis $\lambda_{\text{max}}(\text{THF})/\text{nm}$ ($\epsilon/\text{M}^{-1}\text{cm}^{-1}$): 315 (7700), 302 (11100), 290 (9500), 247 (24000). UV-Vis $\lambda_{\text{max}}(\text{DCM})/\text{nm}$ ($\epsilon/\text{M}^{-1}\text{cm}^{-1}$): 317 (8600), 302 (11800), 291 (8000), 246 (22900). IR (ATR): $\nu = 1598(\text{s}), 1654(\text{s})$ (C=N stretch) cm^{-1} . ^1H NMR (400 MHz, CDCl_3 , 25 °C): $\delta = 8.45$ (s, 4H, H_{imine}), 7.55 (s, 4H, ArH), 3.87 (br s, 8H, NCH_2), 2.06 (br s, 8H, CH_2), 1.37 (s, 18H, $\text{C}(\text{CH}_3)_3$) ppm. $^{13}\text{C}\{^1\text{H}\}$ NMR (101 MHz, CDCl_3 , 25 °C): $\delta = 164.8$ (s, ArC), 163.5 (s, C_{imine}), 153.3 (s, ArC), 125.5 (s, ArCH), 120.2 (d, (2 CF_3 peaks missing) $^1J_{\text{FC}} = 320.2$ Hz, CF_3), 59.8 (s, NCH_2), 35.4 (s, $\text{C}(\text{CH}_3)_3$), 30.5 (s, $\text{C}(\text{CH}_3)_3$), 27.6 (s, CH_2) ppm. $^{19}\text{F}\{^1\text{H}\}$ NMR (376 MHz, CDCl_3 , 25 °C): $\delta = -78.6$ (s, CF_3) ppm. ESI-MS 773.8 m/z [$^{4\text{H}}\text{PDAI}_2\text{Ba}(\text{OTf})$] $^+$.

CRediT authorship contribution statement

Laura M. Thierer: Conceptualization, Investigation, Validation, Formal analysis, Writing - original draft, Writing - review & editing, Visualization. **Qiuran Wang:** Investigation. **Sam H. Brooks:** Investigation. **Peng Cui:** Investigation. **Jia Qi:** Investigation. **Michael R. Gau:** Investigation, Formal analysis. **Brian C. Manor:** Investigation, Formal analysis. **Patrick J. Carroll:** Investigation, Formal analysis. **Neil C. Tomson:** Conceptualization, Writing - review & editing, Visualization, Supervision, Funding acquisition.

Declaration of Competing Interest

The authors declare that they have no known competing financial interests or personal relationships that could have appeared to influence the work reported in this paper.

Acknowledgements

We acknowledge Prof. Gary Molander for the use of the FTIR instrument, Dr. Charles W. Ross III for his support of the Mass Spectrometer as well as Dr. Jun Gu, Dr. George Furst, the National Science Foundation Major Research Instrumentation Program (award NSF CHE-1827457) and the Vagelos Institute for Energy Science and Technology (VIEST) for purchase and maintenance of the NEO400 NMR instrumentation. We thank the University of Pennsylvania, donors of the American Chemical Society Petroleum Research Fund (57346-DNI3) and the National Institute of General Medical Sciences of the National Institutes of Health (R35GM128794) for financial support.

Appendix A. Supplementary data

Supplementary crystallographic data for all crystal structures can be obtained free of charge via <http://www.ccdc.cam.ac.uk/conts/retrieving.html>, or from the Cambridge Crystallographic Data Centre, 12 Union Road, Cambridge CB2 1EZ, UK; fax: (+44) 1223-336-033; or e-mail: deposit@ccdc.cam.ac.uk. Supplementary data to this article can be found online at <https://doi.org/10.1016/j.poly.2021.115044>.

References

- [1] L.S. Morris, M.I. Childers, G.W. Coates, Bimetallic chromium catalysts with chain transfer agents: a route to isotactic poly(propylene oxide)s with narrow dispersities, *Angew. Chem. Int. Ed.* 57 (2018) 5731–5734.
- [2] T.S. Hollingsworth, R.L. Hollingsworth, T. Rosen, S. Groysman, Zinc bimetallics supported by a xanthene-bridged dinucleating ligand: synthesis, characterization, and lactide polymerization studies, *RSC Adv.* 7 (2017) 41819–41829.
- [3] A. Thevenon, C. Romain, M.S. Bennington, A.J.P. White, H.J. Davidson, S. Brooker, C.K. Williams, Dizinc lactide polymerization catalysts: hyperactivity by control of ligand conformation and metallic cooperativity, *Angew. Chem. Int. Ed.* 55 (2016) 8680–8685.
- [4] J. Sampson, G. Choi, M.N. Akhtar, E.A. Jaseer, R. Theravalappil, H.A. Al-Muallem, T. Agapie, Olefin polymerization by dinuclear zirconium catalysts based on rigid teraryl frameworks: effects on tacticity and copolymerization behavior, *Organometallics* 36 (2017) 1915–1928.
- [5] R.J. Somerville, L.V.A. Hale, E. Gómez-Bengoa, J. Burés, R. Martin, Intermediacy of Ni–Ni species in sp^2 C–O bond cleavage of aryl esters: relevance in catalytic C–Si bond formation, *J. Am. Chem. Soc.* 140 (2018) 8771–8780.
- [6] Y.-Y. Zhou, C. Uyeda, Catalytic reductive [4 + 1]-cycloadditions of vinylidenes and dienes, *Science* 363 (2019) 857–862.
- [7] T.C. Davenport, T.D. Tilley, Dinuclear first-row transition metal complexes with a naphthyridine-based dinucleating ligand, *Dalton Trans.* 44 (2015) 12244–12255.
- [8] L. Clowes, C. Redshaw, D.L. Hughes, Vanadium-based pro-catalysts bearing depleted 1,3-calix[4]arenes for ethylene or ϵ -caprolactone polymerization, *Inorg. Chem.* 50 (2011) 7838–7845.
- [9] D. Ghorai, L.H. Finger, G. Zanon, L. Ackermann, Bimetallic nickel complexes for aniline C–H alkylations, *ACS Catal.* 8 (2018) 11657–11662.
- [10] R.B. Siedschlag, V. Bernales, K.D. Vogiatzis, N. Planas, L.J. Clouston, E. Bill, L. Gagliardi, C.C. Lu, Catalytic silylation of dinitrogen with a dicobalt complex, *J. Am. Chem. Soc.* 137 (2015) 4638–4641.
- [11] H. Isobe, K. Tanaka, J.-R. Shen, K. Yamaguchi, Water oxidation chemistry of a synthetic dinuclear ruthenium complex containing redox-active quinone ligands, *Inorg. Chem.* 53 (2014) 3973–3984.
- [12] K. Arashiba, E. Kinoshita, S. Kuriyama, A. Eizawa, K. Nakajima, H. Tanaka, K. Yoshizawa, Y. Nishibayashi, Catalytic reduction of dinitrogen to ammonia by use of molybdenum-nitride complexes bearing a tridentate triphosphine as catalysts, *J. Am. Chem. Soc.* 137 (2015) 5666–5669.
- [13] D. Wang, S.V. Lindeman, A.T. Fiedler, Bimetallic complexes supported by a redox-active ligand with fused pincer-type coordination sites, *Inorg. Chem.* 54 (2015) 8744–8754.
- [14] U.R. Pokharel, F.R. Fronczek, A.W. Maverick, Reduction of carbon dioxide to oxalate by a binuclear copper complex, *Nat. Commun.* 5 (2014) 5883.
- [15] T. Liu, M.R. Gau, N.C. Tomson, Mimicking the constrained geometry of a nitrogen-fixation intermediate, *J. Am. Chem. Soc.* 142 (2020) 8142–8146.
- [16] P. Ghosh, M. Quiroz, N. Wang, N. Bhuvanesh, M.Y. Darensbourg, Complexes of $MN_2S_2Fe(\eta^5-C_5R_5)(CO)$ as platform for exploring cooperative heterobimetallic effects in HER electrocatalysis, *Dalton Trans.* 46 (2017) 5617–5624.
- [17] A.R. Corcos, J.S. Pap, T. Yang, J.F. Berry, A synthetic oxygen atom transfer photocycle from a diruthenium oxoanion complex, *J. Am. Chem. Soc.* 138 (2016) 10032–10040.
- [18] C.U. Perotto, C.L. Sodipo, G.J. Jones, J.P. Tidey, A.J. Blake, W. Lewis, E.S. Davies, J. McMaster, M. Schröder, Heterobimetallic [NiFe] complexes containing mixed CO/CN ligands: analogs of the active site of the [NiFe] hydrogenases, *Inorg. Chem.* 57 (2018) 2558–2569.
- [19] R. Angamuthu, P. Byers, M. Lutz, A.L. Spek, E. Bouwman, Electrocatalytic CO_2 conversion to oxalate by a copper complex, *Science* 327 (2010) 313–315.
- [20] A.L. Gavrilova, B. Bosnich, Principles of mononucleating and binucleating ligand design, *Chem. Rev.* 104 (2004) 349–384.
- [21] K.M. Van Heuvelen, M.T. Kieber-Emmons, C.G. Riordan, T.C. Brunold, Spectroscopic and computational studies of a *trans*- μ -1,2-disulfido-bridged dinickel species, $[(tmc)Ni_2(S_2)](OTf)_2$: comparison of end-on disulfido and peroxo bonding in $(Ni^{II})_2$ and $(Cu^{II})_2$ species, *Inorg. Chem.* 49 (2010) 3104–3112.
- [22] M.A. Sainna, D. Singh, D. Kumar, S.P. de Visser, A trimetal carbene with reactivity reminiscent of Fischer-Tropsch catalysis, *Organometallics* 34 (2015) 1651–1660.
- [23] S. Suseno, C.C.L. McCrory, R. Tran, S. Gul, J. Yano, T. Agapie, Molecular mixed-metal manganese oxido cubanes as precursors to heterogeneous oxygen evolution catalysts, *Chemistry – A Eur. J.* 21 (2015) 13420–13430.
- [24] M.R. Halvagar, P.V. Soltsev, H. Lim, B. Hedman, K.O. Hodgson, E.I. Solomon, C. J. Cramer, W.B. Tolman, Hydroxo-bridged dicopper(II, III) and -(III, III) complexes: models for putative intermediates in oxidation catalysis, *J. Am. Chem. Soc.* 136 (2014) 7269–7272.
- [25] J.R. Pankhurst, S. Paul, Y. Zhu, C.K. Williams, J.B. Love, Polynuclear alkoxy–zinc complexes of bowl-shaped macrocycles and their use in the copolymerisation of cyclohexene oxide and CO_2 , *Dalton Trans.* 48 (2019) 4887–4893.
- [26] P. Cui, Q. Wang, S.P. McCollom, B.C. Manor, P.J. Carroll, N.C. Tomson, Ring-size-modulated reactivity of putative dicobalt-bridging nitrides: C–H activation versus phosphinimide formation, *Angew. Chem. Int. Ed.* 56 (2017) 15979–15983.
- [27] Q. Wang, S. Zhang, P. Cui, A.B. Weberg, L.M. Thierer, B.C. Manor, M.R. Gau, P.J. Carroll, N.C. Tomson, Interdependent metal–metal bonding and ligand redox-activity in a series of dinuclear macrocyclic complexes of iron, cobalt, and nickel, *Inorganic Chem.* 59 (2020) 4200–4214.
- [28] S. Zhang, Q. Wang, L.M. Thierer, A.B. Weberg, M.R. Gau, P.J. Carroll, N.C. Tomson, Tuning metal–metal interactions through reversible ligand folding in a series of dinuclear iron complexes, *Inorg. Chem.* 58 (2019) 12234–12244.
- [29] M. Rezaeivala, H. Keypour, Schiff base and non-Schiff base macrocyclic ligands and complexes incorporating the pyridine moiety – the first 50 years, *Coord. Chem. Rev.* 280 (2014) 203–253.
- [30] S.M. Nelson, C.V. Knox, M. McCann, M.G.B. Drew, Metal-ion-controlled transamination in the synthesis of macrocyclic Schiff-base ligands. Part 1. Reactions of 2,6-diacetylpyridine and dicarbonyl compounds with 3,6-dioxaoctane-1,8-diamine, *J. Chem. Soc., Dalton Trans.* (1981) 1669–1677.
- [31] J. de O. Cabral, M.F. Cabral, W.J. Cummins, M.G.B. Drew, A. Rodgers, S.M. Nelson, Hexagonal bipyramidal alkaline earth and lead(II) complexes of a hexa-imine macrocyclic ligand, *Inorganica Chimica Acta*, 30 (1978) L313–L316.
- [32] C. Harding, D. McDowell, J. Nelson, S. Raghunathan, C. Stevenson, M.G.B. Drew, P.C. Yates, Single-atom [double bond played left]NCS bridging in binuclear complexes of Mn, Fe Co, Ni, and Cu of macrocyclic 20- and 22-membered ligands: a spectroscopic, crystallographic, and molecular mechanics study, *J. Chem. Soc., Dalton Trans.* (1990) 2521–2533.
- [33] B.P. Murphy, J. Nelson, S.M. Nelson, M.G.B. Drew, P.C. Yates, Binucleating N_6 24- and 26-membered macrocyclic ligands. Part 1. Dilead complexes: X-ray crystal structure determination of a macrocyclic dilead complex containing nitrogen-only bridging thiocyanate, *J. Chem. Soc., Dalton Trans.* (1987) 123–127.
- [34] M.G.B. Drew, J. de O. Cabral, M.F. Cabral, F.S. Esho, S.M. Nelson, Alkaline earth, lead(II), and cadmium(II) complexes of a nitrogen analogue of [18]annulene; X-ray crystal structure of the lead and cadmium complexes, *J. Chem. Soc., Chem. Commun.*, (1979) 1033–1035.
- [35] S.M. Nelson, F.S. Esho, M.G.B. Drew, Metal-ion controlled reactions of 2,6-diacetylpyridine with 1,2-di-aminoethane and 2,6-diformylpyridine with o-phenylenediamine and the crystal and molecular structure of a pentagonal pyramidal cadmium(II) complex containing unidentate o-phenylenediamine, *J. Chem. Soc., Dalton Trans.* (1982) 407–415.
- [36] M.G.B. Drew, J. Nelson, S.M. Nelson, Metal-ion-controlled transamination in the synthesis of macrocyclic Schiff-base ligands. Part 2. Stepwise synthesis, ring expansion/contraction, and the crystal and molecular structure of a ten-co-ordinate barium(II) complex, *J. Chem. Soc., Dalton Trans.* (1981) 1678–1684.
- [37] S.M. Nelson, Binuclear complexes of macrocyclic schiff base ligands as hosts for small substrate molecules, *Inorg. Chim. Acta* 62 (1982) 39–50.
- [38] M.G.B. Drew, C.V. Knox, S.M. Nelson, Metal-ion template effects in the synthesis of polydentate Schiff-base ligands. Part 1. Complexes of a potentially octadentate N_6O_2 ligand and the crystal and molecular structure of a ten-co-ordinate barium(II) complex, *J. Chem. Soc., Dalton Trans.* (1980) 942–948.
- [39] V. Alexander, Design and synthesis of macrocyclic ligands and their complexes of lanthanides and actinides, *Chem. Rev.* 95 (1995) 273–342.
- [40] E.D. Reinhart, R.F. Jordan, Template-free synthesis of a macrocyclic bis(pyridine-dienamine) proligand and metal complexes of its bis(pyridine-dienimine) and bis(pyridine-dienamido) forms, *Inorg. Chem.* 58 (2019) 15466–15478.
- [41] J.W. Beattie, D.J. SantaLucia, D.S. White, S. Groysman, Oxalate-templated synthesis of di-zinc macrocycles, *Inorg. Chim. Acta* 460 (2017) 8–16.
- [42] S.M. Nelson, Developments in the synthesis and coordination chemistry of macrocyclic Schiff base ligands, *Pure Appl. Chem.* 52 (1980) 2461–2476.
- [43] S. Nüchel, P. Burger, Transition metal complexes with sterically demanding ligands, 3. Synthetic access to square-planar terdentate pyridine–diimine rhodium(I) and iridium(I) methyl complexes: successful detour via reactive triflate and methoxide complexes, *Organometallics* 20 (2001) 4345–4359.
- [44] D. Gygi, S.J. Hwang, D.G. Nocera, Scalable syntheses of 4-substituted pyridine-diiimines, *J. Organic Chem.* 82 (2017) 12933–12938.
- [45] L. Zhang, Y. Tang, Z. Han, K. Ding, Lutidine-based chiral pincer manganese catalysts for enantioselective hydrogenation of ketones, *Angew. Chem. Int. Ed.* 58 (2019) 4973–4977.

- [46] B. Su, J. Zhao, Y. Cui, Y. Liang, W. Sun, Controlled synthesis of 2-acetyl-6-carbethoxypyridine and 2,6-diacetylpyridine from 2,6-dimethylpyridine, *Synth. Commun.* 35 (2005) 2317–2324.
- [47] K.-K. Yu, K. Li, J.-T. Hou, X.-Q. Yu, Coumarin-TPA derivative: a reaction-based ratiometric fluorescent probe for Cu(I), *Tetrahedron Lett.* 54 (2013) 5771–5774.
- [48] N.T. Coogan, M.A. Chimes, J. Raftery, P. Mocilac, M.A. Denecke, Regioselective synthesis of V-shaped bistriazinyl-phenanthrolines, *J. Organic Chem.* 80 (2015) 8684–8693.
- [49] National Research Council, *Prudent Practices in the Laboratory: Handling and Disposal of Chemicals*, The National Academies Press, Washington, DC, 1995.
- [50] N.K. Nandwana, O.P.S. Patel, M.R. Srivathsa, A. Kumar, Dual role of glyoxal in metal-free dicarbonylation reaction: synthesis of symmetrical and unsymmetrical dicarbonyl imidazoheterocycles, *ACS Omega* 4 (2019) 10140–10150.
- [51] J.L. Galman, D. Steadman, L.D. Haigh, H.C. Hailes, Investigating the reaction mechanism and organocatalytic synthesis of α , α' -dihydroxy ketones, *Org. Biomol. Chem.* 10 (2012) 2621–2628.
- [52] A. Panigrahi, J. Dhineshkumar, K.R. Prabhu, Iodine-Catalyzed C–H functionalization of cyclopentenedione with benzamidine: a double dehydrogenative oxidative cyclization to access fused imidazoles, *Adv. Synth. Catal.* 362 (2020) 2466–2473.
- [53] J.A. McCleverty, T.J. Meyer (Eds.), *Comprehensive Coordination Chemistry II: From Biology to Nanotechnology*, Elsevier Ltd., Amsterdam, 2003, pp. 515–555.
- [54] C. Römlt, T. Weyhermüller, K. Wieghardt, Structural characteristics of redox-active pyridine-1,6-diimine complexes: electronic structures and ligand oxidation levels, *Coord. Chem. Rev.* 380 (2019) 287–317.
- [55] G.J.P. Britovsek, V.C. Gibson, S.K. Spitzmesser, K.P. Tellmann, A.J.P. White, D.J. Williams, Cationic 2,6-bis(imino)pyridine iron and cobalt complexes: synthesis, structures, ethylene polymerisation and ethylene/polar monomer co-polymerisation studies, *J. Chem. Soc., Dalton Trans.* (2002) 1159–1171.
- [56] B. de Bruin, E. Bill, E. Bothe, T. Weyhermüller, K. Wieghardt, Molecular and electronic structures of bis(pyridine-2,6-diimine)metal complexes $[ML_2](PF_6)_n$ ($n = 0, 1, 2, 3$; $M = Mn, Fe, Co, Ni, Cu, Zn$), *Inorg. Chem.* 39 (2000) 2936–2947.
- [57] J. Nelson, B.P. Murphy, M.G.B. Drew, P.C. Yates, S.M. Nelson, Binucleating N_6 24- and 26-membered macrocyclic ligands. Part 2. Transition-metal homo- and hetero-binuclear complexes: X-ray crystallographic structure determination of a lead–manganese heterobinuclear complex, *J. Chem. Soc., Dalton Trans.* (1988) 1001–1010.
- [58] Structure search, CSD database 2019.3.
- [59] J.B. Lambert, E.P. Mazzola, *Nuclear Magnetic Resonance Spectroscopy: An Introduction to Principles, Applications, and Experimental Methods*, Pearson/Prentice Hall, Upper Saddle River, NJ, 2004.
- [60] T.W. Myers, T.J. Sherbow, J.C. Fettinger, L.A. Berben, Synthesis and characterization of bis(imino)pyridine complexes of divalent Mg and Zn, *Dalton Trans.* 45 (2016) 5989–5998.
- [61] F.R. Simões, M.G. Xavier, 6 – Electrochemical Sensors, in: A.L. Da Róz, M. Ferreira, F. de Lima Leite, O.N. Oliveira (Eds.) *Nanoscience and its Applications*, William Andrew Publishing, 2017, pp. 155–178.
- [62] A. Arnold, T.J. Sherbow, R.I. Saylor, R.D. Britt, E.J. Thompson, M.T. Muñoz, J.C. Fettinger, L.A. Berben, Organic electron delocalization modulated by ligand charge states in $[L_2M]^{n+}$ complexes of group 13 ions, *J. Am. Chem. Soc.* 141 (2019) 15792–15803.
- [63] Peak intensities of the square wave voltammograms correspond to the differential current between the reduction and oxidation events and are therefore expected to be proportional to the number of electrons transferred with each event; however, the quasi-reversible and irreversible behavior of the $nR[M]$ complexes is expected to dampen the response signal.
- [64] C.C. Lu, E. Bill, T. Weyhermüller, E. Bothe, K. Wieghardt, Neutral bis(α -iminopyridine)metal complexes of the first-row transition ions (Cr, Mn, Fe Co, Ni, Zn) and their monocationic analogues: mixed valency involving a redox noninnocent ligand system, *J. Am. Chem. Soc.* 130 (2008) 3181–3197.
- [65] R.M. Haas, Z. Hern, S. Sproules, C.R. Hess, An unsymmetric ligand framework for noncoupled homo- and heterobimetallic complexes, *Inorg. Chem.* 56 (2017) 14738–14742.
- [66] Y.-W. Dong, R.-Q. Fan, W. Chen, H.-J. Zhang, Y. Song, X. Du, P. Wang, L.-G. Wei, Y.-L. Yang, Luminescence properties of a Zn(II) supramolecular framework: easily tunable optical properties by variation of the alkyl substitution of (E)-N-(pyridine-2-ylethylidene)arylamine ligands, *RSC Adv.* 6 (2016) 110422–110432.
- [67] A. Saha Roy, P. Saha, P. Mitra, S. Sundar Maity, S. Ghosh, P. Ghosh, Unsymmetrical diimine chelation to M(II) ($M = Zn, Cd, Pd$): atropisomerism, π - π stacking and photoluminescence, *Dalton Trans.* 40 (2011) 7375–7384.
- [68] R.-Q. Fan, D.-S. Zhu, Y. Mu, G.-H. Li, Y.-L. Yang, Q. Su, S.-H. Feng, Syntheses, structures, and luminescent properties of [Bis(iminoalkyl)pyridine]cadmium (II) complexes, *Eur. J. Inorg. Chem.* 2004 (2004) 4891–4897.
- [69] B.R. Reed, S.A. Stojan, R.L. Lord, S. Groysman, The aldimine effect in bis(imino)pyridine complexes: non-planar nickel(II) complexes of a bis(aldimino)pyridine ligand, *Chem. Commun.* 51 (2015) 6496–6499.
- [70] T.M. Smit, A.K. Tomov, G.J.P. Britovsek, V.C. Gibson, A.J.P. White, D.J. Williams, The effect of imine-carbon substituents in bis(imino)pyridine-based ethylene polymerisation catalysts across the transition series, *Catal. Sci. Technol.* 2 (2012) 643–655.
- [71] S.K. Russell, C. Milsmann, E. Lobkovsky, T. Weyhermüller, P.J. Chirik, Synthesis, electronic structure, and catalytic activity of reduced bis(aldimino)pyridine iron compounds: experimental evidence for ligand participation, *Inorg. Chem.* 50 (2011) 3159–3169.
- [72] D.M. Lovett, L.M. Thierer, E.E.P. Santos, R.L. Hardie, W.G. Dougherty, N.A. Piro, W.S. Kassel, B.M. Cromer, E.B. Coughlin, D.L. Zubris, Structural analysis of imino- and amino-pyridine ligands for Ni(II): Precatalysts for the polymerization of ethylene, *J. Organomet. Chem.* 863 (2018) 44–53.
- [73] P.H.M. Budzelaar, B. de Bruin, A.W. Gal, K. Wieghardt, J.H. van Lenthe, Metal-to-ligand electron transfer in diiminopyridine complexes of Mn–Zn. A theoretical study, *Inorganic Chem.* 40 (2001) 4649–4655.
- [74] W.Q. Ong, H. Zhao, X. Fang, S. Woen, F. Zhou, W. Yap, H. Su, S.F.Y. Li, H. Zeng, Encapsulation of conventional and unconventional water dimers by water-binding foldamers, *Org. Lett.* 13 (2011) 3194–3197.
- [75] Bruker SAINT v8.38A; Bruker AXS Inc.: Madison, WI, 2014.
- [76] CrysAlisPro 1.171.40.53; Rigaku Oxford Diffraction, Rigaku Corporation, Oxford, UK, 2019.
- [77] G. Sheldrick, SHELXT – integrated space-group and crystal-structure determination, *Acta Crystallogr. Section A* 71 (2015) 3–8.
- [78] F. Neese, The ORCA program system, *WIREs Comput. Mol. Sci.* 2 (2012) 73–78.
- [79] S. Grimme, Semiempirical GGA-type density functional constructed with a long-range dispersion correction, *J. Comput. Chem.* 27 (2006) 1787–1799.
- [80] S. Grimme, J. Antony, S. Ehrlich, H. Krieg, A consistent and accurate ab initio parametrization of density functional dispersion correction (DFT-D) for the 94 elements H–Pu, *J. Chem. Phys.* 132 (2010) 154104.
- [81] S. Grimme, S. Ehrlich, L. Goerigk, Effect of the damping function in dispersion corrected density functional theory, *J. Comput. Chem.* 32 (2011) 1456–1465.
- [82] A. Schäfer, H. Horn, R. Ahlrichs, Fully optimized contracted Gaussian basis sets for atoms Li to Kr, *J. Chem. Phys.* 97 (1992) 2571–2577.
- [83] A. Schäfer, C. Huber, R. Ahlrichs, Fully optimized contracted Gaussian basis sets of triple zeta valence quality for atoms Li to Kr, *J. Chem. Phys.* 100 (1994) 5829–5835.
- [84] F. Weigend, R. Ahlrichs, Balanced basis sets of split valence, triple zeta valence and quadruple zeta valence quality for H to Rn: design and assessment of accuracy, *PCCP* 7 (2005) 3297–3305.
- [85] E.F. Pettersen, T.D. Goddard, C.C. Huang, G.S. Couch, D.M. Greenblatt, E.C. Meng, T.E. Ferrin, UCSF Chimera—a visualization system for exploratory research and analysis, *J. Comput. Chem.* 25 (2004) 1605–1612.